

Long-Term Evolution of Slowly Rotating Collapsar in Special Relativistic Magnetohydrodynamics

Seiji Harikae^{1,2}, Tomoya Takiwaki³, and Kei Kotake^{2,3}

¹*Department of Astronomy, The Graduate School of Science, University of Tokyo, 7-3-1 Hongo, Bunkyo-ku, Tokyo, 113-0033, Japan*

²*Division of Theoretical Astronomy, National Astronomical Observatory of Japan, 2-21-1, Osawa, Mitaka, Tokyo, 181-8588, Japan*

³*Center for Computational Astrophysics, National Astronomical Observatory of Japan, 2-21-1, Osawa, Mitaka, Tokyo, 181-8588, Japan*

seiji.harikae@nao.ac.jp

ABSTRACT

We present our numerical results of two-dimensional magnetohydrodynamic (MHD) simulations of the collapse of rotating massive stars in light of the collapsar model of gamma-ray bursts (GRBs). Pushed by recent evolution calculations of GRB progenitors, we focus on lower angular momentum of the central core than the ones taken mostly in previous studies. By performing special relativistic simulations including both realistic equation of state and neutrino cooling, we follow a long-term evolution of the slowly rotating collapsars up to ~ 10 s, accompanied by the formation of jets and accretion disks. Our results show that for the GRB progenitors to function as collapsars, there is a critical initial angular momentum, below which matter is quickly swallowed to the central objects, no accretion disks and no MHD outflows are formed. When larger than the criteria, we find the launch of the MHD jets in the following two ways. For models with stronger initial magnetic fields, the magnetic pressure amplified inside the accretion disk can drive the MHD outflows, which makes the strong magnetic explosions like a 'magnetic tower'. For models with weaker initial magnetic fields, the magnetic tower stalls first and the subsequent MHD outflows are produced by the magnetic twisting of the turbulent inflows of the accreting material from the equatorial to the polar regions. Regardless of the difference in the formation, the jets can attain only mildly relativistic speeds with the explosion energy less

than 10^{49} erg. To obtain stronger neutrino energy depositions in the polar funnel regions heated from the accretion disk, we find that smaller initial angular momentum is favorable. This is because the gravitational compression makes the temperature of the disk higher. Due to high neutrino opacity inside the disk, we find that the luminosities of ν_e and $\bar{\nu}_e$ become almost comparable, which is advantageous for making the energy deposition rate larger. We discuss how the energy deposition can be as efficient as the magnetically-driven processes for energizing jets. Among the computed models, we suggest that the model with the initial angular momentum of $j \sim 1.5j_{\text{iso}}$ (j_{iso} : the angular momentum of the last stable orbit) and with initial magnetic field strength of $\sim 10^{10}$ G, provides a most plausible condition for making fireballs for GRBs, because such model is appropriate not only for producing the MHD outflows quickly by the magnetic towers, but also for obtaining the stronger neutrino heating in the evacuated polar funnel.

Subject headings: collapsar: black hole, disk — supernovae: collapse, rotation — magnetars: pulsars, magnetic field — methods: numerical — MHD — special relativity — gamma rays: bursts

1. Introduction

Gamma-ray bursts (GRBs) are one of the most energetic phenomena in the universe. Accumulating observations discovered such as by *Swift*¹ and *HETE-2*² show that GRBs are basically categorized into two, namely short-hard and long-soft bursts (e.g., Nakar (2007) for review). More surprisingly, GRBs with some mixed features of the two types have been reported (e.g., Gehrels et al. (2006), Gal-Yam et al. (2006)). The mystery of their central engines seems to be thickening, which have long puzzled astrophysicists since the accidental discovery in the late sixties (e.g., Meszaros (2006), for review). Speaking about the long-duration GRBs, a number of their host galaxies have been identified as metal poor galaxies (Savaglio et al. 2006; Stanek et al. 2006, and reference therein). The preponderance of short-lived massive star formation in such young galaxies, as well as the identification of SN Ib/c light curves in some bursts, has provided strong support to identify a massive stellar collapse as an origin of the long GRBs (Paczynski 1998; Galama et al. 1998; Hjorth et al. 2003; Stanek et al. 2003). The duration of the long bursts may correspond to the accretion of debris

¹<http://www.swift.psu.edu/>

²<http://space.mit.edu/HETE/>

falling into the central black hole (BH)(Piro et al. 1998), which suggests the observational consequence of the BH formation likewise the supernova of neutron star formation. Pushed by those observations, the so-called collapsar has received quite some interest for the central engines of the long GRBs (Woosley 1993; Paczynski 1998; MacFadyen & Woosley 1999).

In the collapsar model, the central cores with significant angular momentum collapse into a BH. Neutrinos emitted from the accretion disk around the BH heat the matter of the funnel region of the disk, to launch the GRB outflows. The relativistic outflows are expected to ultimately form a fireball, which is good for explaining the observed afterglow (e.g., Piran (1999)). In addition, it is suggested that the strong magnetic fields in the cores of order of 10^{15}G play also an active role both for driving the magneto-driven jets and for extracting a significant amount of energy from the central engine (e.g., Wheeler et al. (2000); Thompson et al. (2004); Uzdensky & MacFadyen (2007a) and see references therein).

To obtain clear understanding of such scenarios, it is ultimately necessary to perform stellar core-collapse simulations, which trace all the phases in a consistent manner starting from the stellar core-collapse, core-bounce, shock-stall, stellar explosion (phase 1) or BH formation and the formation of accretion disk (phase 2), energy deposition to the funnel region by neutrinos and/or magnetic fields (phase 3), to the launching of the fireballs (phase 4). Here for convenience we call each stage as phase 1, 2, etc. The requirement for the numerical modeling to this end is highly computationally expensive, which necessitates the multidimensional magnetohydrodynamic(MHD) simulations not only with general relativity for handling the BH formation, but also with the multi-angle neutrino transfer for treating highly anisotropic neutrino radiation from the disks. Thus various approximate approaches have been undertaken. All the studies, which we will mention below, are complimentary in the sense that the different epochs are focused on, with the different initial conditions for the numerical modeling being taken.

As for the phase 1, the roles of rapid rotation and magnetic fields have been elaborately investigated to study the formation of magnetars and its implications to the collapsars (e.g., Takiwaki et al. (2004); Kotake et al. (2004); Sawai et al. (2005); Obergaulinger et al. (2006); Suwa et al. (2007); Burrows et al. (2007); Takiwaki et al. (2009) and collective references in Kotake et al. (2006)). After the failed or weak explosion in the postbounce phase, the accretion to the central objects may lead to the formation of a BH (phase 2), which several general relativistic studies have focused on (Shibata et al. 2006; Sekiguchi & Shibata 2007). Treating the BH as an absorbing boundary or using the fixed metric approaches, the numerical studies of the phase 3 are concerned with the initiation of the outflows from the funnel region of the disk to the acceleration of the jets as a result of the neutrino heating and/or MHD processes till the jets become mildly relativistic. Numerical studies of the phase 4 are

mainly concerned with the dynamics later on, namely, the jet propagation to the breakout from the star, when the acceleration of the jets to the high Lorentz factor is expected (see, e.g., Aloy et al. (2000); Zhang et al. (2003); Mizuno et al. (2007) and references therein).

Here we focus on the phase 3, which has also been extensively investigated thus far (e.g., MacFadyen & Woosley (1999); Proga et al. (2003b); De Villiers et al. (2005); Hawley & Krolik (2006); Mizuno et al. (2006); Fujimoto et al. (2006); McKinney & Narayan (2007); Komissarov & McKinney (2007); Nagataki et al. (2007); Barkov & Komissarov (2008)). A general outcome of the MHD studies among them (e.g., Proga (2003); Proga et al. (2003b); Mizuno et al. (2006); Fujimoto et al. (2006); Nagataki et al. (2007); Nagataki (2009)) is that if the central progenitor cores have significant angular momentum ($\approx 10^{17}$ cm²/s) with strong magnetic fields ($\gtrsim 10^{11}$ G), magneto-driven jets can be launched strong enough to expel the matter along the rotational axis within several seconds after the onset of collapse. The combination of such rapid rotation and strong magnetic fields is recently considered to be possible for rapidly rotating metal-poor stars, which experience the so-called chemically homogeneous evolution in the main sequence (Woosley & Heger 2006; Yoon & Langer 2005). It should be noted that the angular momentum of those GRB progenitors ($\approx 10^{16}$ cm²/s), albeit not a final answer due to much uncertainty in the stellar mass loss, angular momentum transport, and magnetorotational instability (MRI) (e.g., Vink & de Koter (2005), Detmers et al. (2008)), is relatively smaller than those assumed in most of the previous collapsar simulations. Employing such a GRB progenitor, it was reported by Dessart et al. (2008) based on the 2D radiation MHD core-collapse simulations that too much angular momentum is not favorable for collapsars because the MHD explosions in the immediate postbounce phase are so strong that the BH formations are circumvented.

These situations motivate us to focus on slower rotation of the central core in the context of collapsar models. As for the initial magnetic fields, we choose to explore relatively smaller fields ($\lesssim 10^{10}$ G), which has been less investigated so far. Paying particular attention to the smaller angular momentum, it takes much longer time to amplify the magnetic fields large enough to launch the MHD jets than previously estimated. By performing special relativistic MHD simulations, which enable us to follow a long-term evolution over ~ 10 s, we aim to clarify how the properties and the mechanism of the MHD jets could change with the initial angular momentum and the initial magnetic fields. It is noted here that the long-term simulation could be important for understanding the X-ray flares recently discovered in a number of long GRBs (e.g., Proga & Zhang (2006)). As for the microphysics, we include both realistic equation of state (EOS) and neutrino cooling, which have been often neglected or oversimplified (see, however, Fujimoto et al. (2006); Nagataki et al. (2007)). By doing so, we estimate the neutrino luminosities emitted from the accretion disks, and clarify what conditions are pivotal to make the energy depositions via neutrino pair anni-

lation as efficient as the magnetically-driven processes for energetizing jets. The range of specific angular momentum required for the progenitors of collapsars was predicted to be $3 < j_{16} (\equiv j/10^{16} \text{cm}^2 \text{s}^{-1}) < 20$ by a pioneering collapsar simulation but without MHD (MacFadyen & Woosley 1999). This is because if angular momentum is too small, mass element cannot stay at the last stable orbit, while if too large, mass element cannot fall into compact objects, and thus cannot form disk, suppressing the sufficient energy release for GRBs. Based on our results, we hope to understand how this criterion would change if MHD effects are taken into account.

We summarize the numerical methods in §2. §3 is devoted to the initial models. The main results are described in §4. We summarize our results and discuss their implications in §5. Details of the treatments of neutrino cooling/heating in the framework of special relativity are given in the appendices.

2. Numerical methods

The results presented in this paper are calculated by the MHD code in special relativity (SR) developed by Takiwaki et al. (2009). In the following, we briefly mention the importance of SR for collapsar simulations and summarize shortly the numerical schemes.

SR effects are indispensable not only to follow the propagation of GRB jets in high Lorentz factors, but also to follow the dynamics of infalling material, because their free-fall velocities and rotational velocities become close to the speed of light near the central compact objects. Moreover, the velocity of the Alfvén waves during the jet propagation can be estimated as,

$$v_A = \frac{B}{\sqrt{4\pi\rho}} \sim 10^{10} \text{cm/s} \frac{B/10^{13}\text{G}}{\sqrt{\rho/(10^5\text{g/cm}^3)}}, \quad (1)$$

where ρ and B are the typical density and the magnetic field near along the rotational axis. It can be readily inferred that the Alfvén velocity can exceed the speed of light unphysically in the Newtonian simulation, especially for the regions where the density becomes low and the magnetic fields become strong. Such a situation is ubiquitous for collapsar simulations. Even if the propagation speeds of the jets are only mildly relativistic, we have learned that (at least) SR treatments are quite important for keeping the stable numerical calculations in good accuracy over the longer-term evolution.

The SRMHD part of the code is based on the formalism of De Villiers et al. (2003)(see Takiwaki et al. (2009) for details). To formalize the basic equations, we need two frames; the laboratory frame (we call shortly as lab frame), which is the center of mass system of

the star, and the rest frame of the relativistic fluid. These two frames are related to each other with the usual Lorentz transformation. Before going to the basic equations, we write down the definition of the primary code variables. The state of the relativistic fluid element in the rest frame is described by its density, ρ ; specific energy, e ; velocity, v^i ; and pressure, p . Magnetic fields in the lab frame is described by the 4-vector $\sqrt{4\pi}b^\mu = {}^*F^{\mu\nu}U_\nu$, where ${}^*F^{\mu\nu}$ is the dual tensor of the electro-magnetic field strength tensor and U_ν is the 4-velocity.

The basic equations of the SRMHD code can be described as follows:

$$\frac{\partial D}{\partial t} + \frac{1}{\sqrt{\gamma}}\partial_i\sqrt{\gamma}Dv^i = 0 \quad (2)$$

$$\frac{\partial E}{\partial t} + \frac{1}{\sqrt{\gamma}}\partial_i\sqrt{\gamma}Ev^i = -p\frac{\partial W}{\partial t} - \frac{p}{\sqrt{\gamma}}\partial_i\sqrt{\gamma}Wv^i - \mathcal{L}_\nu \quad (3)$$

$$\begin{aligned} \frac{\partial(S_i - b^tb_i)}{\partial t} + \frac{1}{\sqrt{\gamma}}\partial_j\sqrt{\gamma}(S_iv^j - b_ib^j) &= -\frac{1}{2}(\rho h(Wv_k)^2 - (b_k)^2)\partial_i\gamma^{kk} \\ &\quad - (\rho hW^2 - b^{t2})\partial_i\Phi_{\text{tot}} \\ &\quad - \partial_i\left(p + \frac{\|b\|^2}{2}\right) \end{aligned} \quad (4)$$

$$\frac{\partial(Wb^i - Wb^tv^i)}{\partial t} + \partial_j(Wv^jb^i - Wv^ib^j) = 0 \quad (5)$$

$$\begin{aligned} \partial^k\partial_k\Phi_{\text{poi}} &= 4\pi\left[\rho h(W^2 + (v_k)^2) + 2\left(p + \frac{|b|^2}{2}\right) \right. \\ &\quad \left. - ((b^t)^2 + (b_k)^2)\right] \end{aligned} \quad (6)$$

where $W = \frac{1}{\sqrt{1-v^kv_k}}$, $D = \rho W$, $E = eW$ and $S_i = \rho hW^2v_i$ are the Lorentz boost factor, auxiliary variables correspond to density, energy, and momentum, respectively. All of them are defined in the lab frame. Equations.(2,3,4) represent the mass, energy, and momentum conservations. In Eq.(4) it is noted that the relativistic enthalpy, $h = (1 + e/\rho + p/\rho + |b|^2/\rho)$ includes magnetic energy. Eq.(5) is the induction equation for the magnetic fields. In solving the equation, the method of characteristics is implemented to propagate accurately all modes of MHD waves (see Takiwaki et al. (2009) for details). B^i is the magnetic field in the rest frame, which is related to the one in the lab frame as $B^i = Wb^i - Wb_tv^i$. Here b_t is a time component of the 4-vector of b_μ . Eq.(6) is the Poisson equation for the (self-)gravitational potential of Φ_{poi} . We employ the realistic equation of state based on the relativistic mean field theory (Shen et al. 1998). For lower density regime ($\rho \lesssim 10^{5.5}\text{g cm}^{-3}$), where no data is available in the EOS table with the Shen EOS, we use another EOS, which includes contributions from an ideal gas of nuclei, radiation, and electrons and positrons with

arbitrary degrees of degeneracy (Blinnikov et al. 1996). We carefully connect two EOS at $\rho = 10^{5.5} \text{g cm}^{-3}$ for physical quantities to vary continuous in density at a given temperature.

\mathcal{L}_ν in Eq.(3) is the neutrino luminosity evaluated with a multi-flavor leakage scheme (Epstein & Pethick (1981); Rosswog & Liebendörfer (2003); Kotake et al. (2003)), in which ν_e , $\bar{\nu}_e$, and the heavy-lepton neutrinos, ν_μ , $\bar{\nu}_\mu$, ν_τ , $\bar{\nu}_\tau$ (collectively referred to as ν_X) are taken into account. Electron capture on proton and free nuclei, positron capture on neutron, photo-pair, plasma process are included (Fuller et al. (1985), Takahashi et al. (1978), Itoh et al. 1989, 1990). Furthermore, we update the leakage scheme to include special relativistic corrections for the first time to our knowledge (see Appendix B for details).

Spherical coordinates, (r, θ, ϕ) are used in our simulations and the computational domain is extended over $50\text{km} \leq r \leq 30000\text{km}$ and $0 \leq \theta \leq \pi/2$ and covered with $300(r) \times 40(\theta)$ meshes with the assumption of axial and equatorial symmetry. As in MacFadyen & Woosley (1999); Fujimoto et al. (2006), we adopt an absorptive inner boundary condition at 50 km. Together with SR treatment of MHD, this inner boundary, albeit taken to be large, allows us to explore the long-term evolution of collapsars. Note that we do not necessarily assume the formation of BH inside, but only assume that the central region would not affect the regions outside. One interpretation of the position of the inner-boundary could be a surface of the standing accretion shock waves produced after bounce. In §5.3, by counting the accreted mass in the central objects when the simulations terminate, we will discuss what they could be, namely the neutron stars or the BHs.

The total gravitational potential in Eq. (4) is

$$\Phi_{\text{tot}} = \Phi_{\text{PW}} + \Phi_{\text{poi}}, \quad (7)$$

where Φ_{PW} mimics the contribution from strong gravity around the central objects (Paczynsky & Wiita 1980). Under the special relativistic modification, this potential has been suggested as useful to reproduce the dynamics outside the last stable orbit in the Schwarzschild metric (Abramowicz et al. (1996); Fukue (2004)). Thus such treatment, albeit very approximate, may not be too bad for our computations (see discussions in §5.3). To achieve further accuracy, we need to perform simulations in curved time-space with general relativistic MHD, which is beyond the scope of this paper.

3. Initial conditions

As for the initial profiles of the collapsing star, we employ the spherical data set of the density, temperature, internal energy, and electron fraction in model 35OC with the mentioned chemically homogeneous evolution (Woosley & Heger 2006). At the the zero age

| Model | B_0 | α | $T/ W $ | $E_{\text{mag}}/ W $ |
|---------|-------------------|----------|------------------------|-------------------------|
| B10J1.0 | 10^{10}G | 1.0 | 5.515×10^{-3} | 2.108×10^{-8} |
| B10J1.5 | 10^{10}G | 1.5 | 1.241×10^{-2} | 2.108×10^{-8} |
| B10J2.0 | 10^{10}G | 2.0 | 2.206×10^{-2} | 2.108×10^{-8} |
| B10J2.5 | 10^{10}G | 2.5 | 3.447×10^{-2} | 2.108×10^{-8} |
| B10J3.0 | 10^{10}G | 3.0 | 4.964×10^{-2} | 2.108×10^{-8} |
| B9J1.0 | 10^9G | 1.0 | 5.515×10^{-3} | 2.108×10^{-10} |
| B9J1.5 | 10^9G | 1.5 | 1.241×10^{-2} | 2.108×10^{-10} |
| B9J2.0 | 10^9G | 2.0 | 2.206×10^{-2} | 2.108×10^{-10} |
| B9J2.5 | 10^9G | 2.5 | 3.447×10^{-2} | 2.108×10^{-10} |
| B9J3.0 | 10^9G | 3.0 | 4.964×10^{-2} | 2.108×10^{-10} |
| B8J1.0 | 10^8G | 1.0 | 5.515×10^{-3} | 2.108×10^{-12} |
| B8J1.5 | 10^8G | 1.5 | 1.241×10^{-2} | 2.108×10^{-12} |
| B8J2.0 | 10^8G | 2.0 | 2.206×10^{-2} | 2.108×10^{-12} |
| B8J2.5 | 10^8G | 2.5 | 3.447×10^{-2} | 2.108×10^{-12} |
| B8J3.0 | 10^8G | 3.0 | 4.964×10^{-2} | 2.108×10^{-12} |

Table 1: Models and Parameters. Model names are labeled by the initial strength of magnetic fields and rotation. B_0 is a constant in Eq.(10), α is the ratio of the specific angular momentum normalized by the one at the last stable orbit in Eq.(8). $T/|W|$ and $E_{\text{mag}}/|W|$ represents the ratio of the rotational energy and the magnetic energy to the absolute value of the gravitational energy, respectively.

main-sequence, the progenitor mass, rotational velocity, and metallicity are $35M_\odot$, $v_\phi = 380\text{km/s}$, and $0.1Z_\odot$, respectively. At the presupernova phase, the stellar mass is striped to be $28.07M_\odot$ due to the mass-loss and the mass of the central iron core is $2.02M_\odot$. Our numerical grid contains inner $8.56M_\odot$ of the star.

Since little is known about the spatial configurations of the rotation and the magnetic fields from the stellar evolution calculations assuming spherical symmetry of the stars, we add the following rotation and magnetic field profiles in a parametric manner to the core mentioned above.

As for the initial angular momentum of the core, we parametrize the strength by the angular momentum of the last stable orbit ($: j_{\text{lso}}$) following Lee & Ramirez-Ruiz (2006); Lopez-Camara et al. (2009); Proga et al. (2003a,b); Proga (2003, 2005) as

$$j = \alpha j_{\text{lso}}(M(R)), \quad (8)$$

where j is the specific angular momentum, $M(R)$ is the spherical mass coordinate, encom-

passing the mass inside radius R , and α is a model parameter. In this study, we set $1 \leq \alpha \leq 3$. Note that, although angular momentum is larger than j_{iso} with this range, it does not assure the formation of the stable disk because of the existence of the slowly rotating matter in the polar regions and relatively large inner boundary of our models. Thus dynamical simulations are necessary to specify the criteria of the disk formation.

As for the initial configuration of the magnetic fields, we assume that the poloidal field is nearly uniform and parallel to the rotational axis inside the core and dipolar outside. For the purpose, we consider the following effective vector potential,

$$A_r = A_\theta = 0, \quad (9)$$

$$A_\phi = \frac{B_0}{2} \frac{r_0^3}{r^3 + r_0^3} r \sin \theta, \quad (10)$$

where $A_{r,\theta,\phi}$ is the vector potential in the r, θ, ϕ direction, respectively, r is the radius, r_0 is the radius of the core, and B_0 is the model constant. We set $r_0 = 3000$ km between the iron core and the silicon layers and change parametrically B_0 as $B_0 = 10^8, 10^9$ and 10^{10} G for each model.

We compute 15 models changing the initial angular momentum and the strength of magnetic fields by varying the value of α and B_0 . Each models are named as BXJY, where X indicates the initial poloidal magnetic field (10^X G), and Y represents the ratio of the specific angular momentum to j_{iso} . For example, B9J1.5 represents the model with $B_0 = 10^9$ and $j = 1.5j_{\text{iso}}$. The model parameters are shown in Table 1. It is noted that $T/|W|$ and $E_{\text{mag}}/|W|$ for the original progenitor of the model 35OC is 2×10^{-3} and 1×10^{-6} , respectively. Thus the model series with J1.0 have almost the same angular momentum with the progenitor. Considering the mentioned uncertainties of the progenitor models, we choose to explore relatively smaller field strength, which has been less investigated so far.

4. Results

Computing 15 models in a longer time stretch than ever among previous collapsar models, we observe a wide variety of the dynamics changing drastically with time. To capture the general properties of all the models, we first pay attention to the time evolutions of the central mass, the mass of the accretion disk, and the neutrino luminosity in the following.

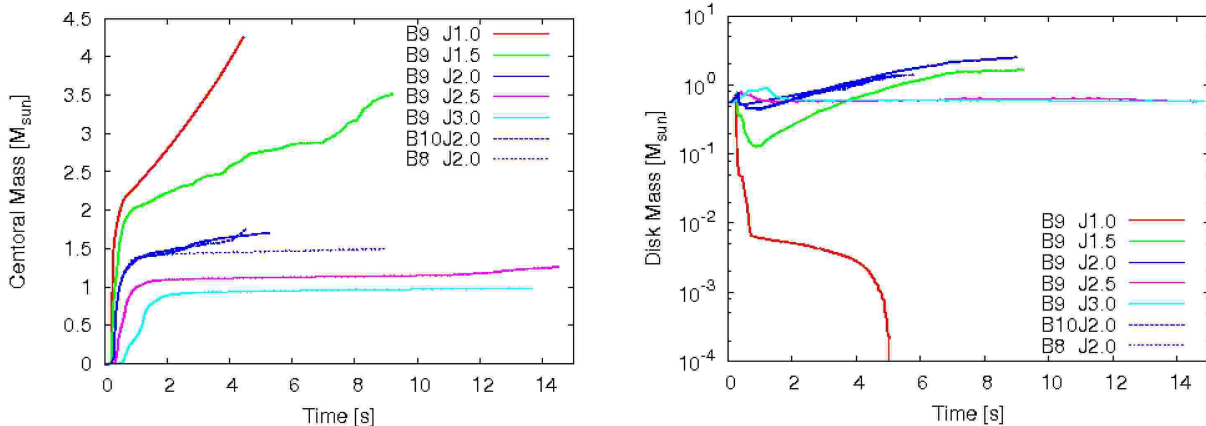


Fig. 1.— Time evolutions of the masses accreting to the central objects (left) and the masses of the accretion disks (right). Top 5 lines of red, green, blue, purple, and water correspond to the models with the same initial magnetic field of 10^9 G but with $j = j_{\text{iso}}, 1.5j_{\text{iso}}, 2j_{\text{iso}}, 2.5j_{\text{iso}},$ and $3j_{\text{iso}}$, respectively. For the case of $j = 2j_{\text{iso}}$ (blue), the dashed, solid, and dotted line show the variation of the initial magnetic fields ($B_0 = 10^{10}, 10^9,$ and 10^8 G), respectively. It can be shown that for rapidly rotating models, the mass accretion rate to the center becomes smaller (left) and the accretion disks become heavier (right). To estimate the disk mass, we count the mass elements which are nearly in the hydrodynamical equilibrium near the equatorial plane.

4.1. General features

4.1.1. Central mass and disk mass

The left panel of Figure 1 shows the time evolution of the central mass for some representative models, where the central mass is defined to be the baryonic mass accreted onto the central object through the inner boundary. It is shown that the central mass grows larger and more quickly for the models with the smaller initial angular momentum. This is simply due to the smaller centrifugal forces. In fact, the slowest rotation model of B9J1.0 shows a fastest increase, and as a result, the mass of the accretion disk becomes lightest (right panel). Such a feature seems close to the so-called dwarf disk, in which matter is swallowed to the center with nearly a free-fall velocity in the equatorial plane (Lee & Ramirez-Ruiz (2006); Lopez-Camara et al. (2009)). Here it should be noted that very rapid growth of the central mass has been predicted to affect the collapsar ability to produce jets (Janiuk et al. 2008; Janiuk & Proga 2008), which we observe actually in our simulations and will be explained in the following section. For all the models with J1.0, on the other hand, we do not observe any MHD jets owing to inefficient winding of the magnetic fields. Moreover neutrino luminosi-

ties from very thin accretion disks for the models is typically about 2 orders-of-magnitudes smaller than for the other models. So, we regard such models as inadequate for the progenitor of collapsars and focus on the models with $j \geq 1.5j_{\text{iso}}$ in the subsequent sections. Here, we define the critical angular momentum to be the minimum angular momentum to form the stable and thick disk. In our case, the critical value is $j = 1.5j_{\text{iso}}$.

From the left panel, it can be also seen that the increase of the central mass becomes slightly larger for models with larger initial magnetic fields (compare blue lines). This is likely due to the angular momentum transport via the magnetic fields, which enhances the matter accretion to the center. However the difference of the initial angular momentum is more decisive to capture the main dynamical features among the computed models, on which we focus in the following.

4.1.2. MHD outflows and neutrino luminosity

To extract the general features furthermore among the models, we focus on the properties of MHD outflows and neutrino luminosities. It is noted that both of them is helpful to understand the energy sources for powering the GRBs namely via magnetic and/or neutrino-heating mechanisms. More specifically speaking, the information of the neutrino luminosity is indispensable to estimate the neutrino energy deposition from the accretion disk. And the formations of MHD outflows is also important, because it can evacuate the funnel for the secondary jets along the rotational axis, which could be the birthplace of relativistic fireballs.

Top column of each cell of Table 2 indicates whether the MHD jets are formed (yes or no indicated by \bigcirc or \times). TYPE I or II indicates the difference of the formation process of the MHD jets, which we will explain in detail from the next section (section 4.2).

The quantities of the middle column show the neutrino luminosity (sum of all the neutrino species ν_e , $\bar{\nu}_e$, and ν_X) estimated at the epoch when the accretion disks becomes stationary(bottom) (e.g., typically ~ 4 sec in Figure 1). We find that the neutrino luminosities become higher for slower rotation models. This is because the accretion disks can attain higher temperatures due to the gravitational compression. It is interesting to note that the luminosities tend to become smaller for strongly magnetized models with relatively smaller angular momentum ($J \leq J_{2.5}$). This is mainly because the gravitational compression is hindered by the magnetic forces confined in the disks. More detailed analysis of the luminosities is given in section 4.3.

| Model Name | J1.5 | J2.0 | J2.5 | J3.0 |
|------------|--|--|---|---|
| B10 | ○ (TYPE II) 1.1×10^{52} erg/s 3.4 s | ○ (TYPE II) 4.5×10^{51} erg/s 5.8 s | ○ (TYPE I) 1.6×10^{50} erg/s 7.7 s | ○ (TYPE I) 9.0×10^{49} erg/s 9.3 s |
| B9 | ○ (TYPE I) 1.6×10^{52} erg/s 9.2 s | ○ (TYPE I) 5.1×10^{51} erg/s 5.3 s | × 1.4×10^{50} erg/s 12 s | × 2.5×10^{49} erg/s 14 s |
| B8 | × 1.8×10^{52} erg/s 4.3 s | × 8.5×10^{51} erg/s 6.0 s | × 1.7×10^{50} erg/s 10 s | × 4.5×10^{49} erg/s 12 s |

Table 2: Properties of MHD jets and neutrino luminosities. Contents of each cell is, whether the MHD jets are formed (yes or no indicated by ○ or ×) with the different formation mechanisms indicated by TYPE I or TYPE II (top), the neutrino luminosity (middle) estimated at the epoch (bottom) when the accretion disks become almost stationary. While the success or failure of the jet-launch depends both on the initial strength of magnetic fields and rotation, the neutrino luminosity is shown to be predominantly determined by the initial rotation rates.

4.2. Formation of Magnetically-dominated Jets

In Table 2, we categorized the launching of the MHD jets in two ways. Here it should be noted that we distinguish the collimated outflow as “ jets ” where their half-opening angle is less than 10° . Before discussing the details of each type in section 4.2.2, we mention the amplification of the toroidal magnetic fields and the subsequent formation of the magnetic outflows from the accretion disks, which precedes the jet formations.

4.2.1. Amplification of magnetic fields and the outflows from accretion disks

Since the initial models investigated here are assumed to have only the poloidal fields (section 3), the key ingredients for amplifying the toroidal fields are the compression of the poloidal fields and the efficient wrapping of them via differential rotations. In addition, MRI should also play an important role, whose wavelength of the fastest growing mode is given by $\lambda \sim 5 \left(\frac{300/\text{s}}{\Omega} \right) \left(\frac{B}{10^{12}\text{G}} \right) \left(\frac{10^{10}\text{g/cm}^3}{\rho} \right)^{1/2}$ km (Balbus & Hawley 1998). Here, putting the typical physical values of the disk, our numerical grids are insufficient to capture MRI at earlier phase when the magnetic field is weak, but can handle it in the later phase when the magnetic field gets stronger. In this sense, the discussion below, which fails to include the

effects of MRI completely, should give a lower bound for the field amplification. Discussions about MRI are given with numerical tests in section 5.4.

Figure 2 shows the distributions of density and poloidal fields of model B9J1.5 at 7.99 s, just before the launch of the MHD outflows from the accretion disk. The density takes its maximum value at around 120 km in the equatorial plane (left panel), in which the poloidal fields are strong because the higher compression is achieved (right panel). The white solid line in the right panel indicates the surface positions of the accretion disk. So the amplifications of the poloidal fields occur most efficiently inside the accretion disk. It is noted here that the disk is gravitationally stable because the adiabatic index (γ) inside the disk becomes greater than $4/3$ due to the contribution of the non-relativistic nucleon ($\gamma = 5/3$) photodissociated from the iron nuclei.

As for the toroidal fields, Figure 3 shows that their amplification rates are highest also inside the disk (right), because the degree of the differential rotation is large there (left). In previous collapsar simulations assuming much larger angular momentum initially (e.g., Proga et al. (2003b); Fujimoto et al. (2006)), it seems to be widely agreed that the differential rotation is a primary agent to amplify the toroidal fields. On the other hand, our results show that for long-term evolution of relatively slow rotation models (see also Proga (2005)), the amplification of the poloidal fields by compression is preconditioned for the amplification of the toroidal fields.

The left panel of Figure 4 shows that the toroidal fields are amplified as high as 10^{16} G inside the disk, where the amplification rate is indeed high (see Figure 3 (right)). The ratio of the magnetic to rotational energy at this moment is about $\sim 10\%$, which is close to the saturation level of the field growth as shown in Shibata et al. (2006). From the right panel, it can be seen that the magneto-driven outflows, in which the magnetic pressure dominates over the matter pressure, are produced in the vicinity of the accretion disk. Looking carefully, the amplification rates are higher near along the equator (Figure 3 (right)) and decrease as the distance to the equator gets larger vertically (perpendicular to the equator). We find that the vertical gradient of the magnetic pressure near the surface of the disk can drive the MHD outflows. It is interesting that the propagation of the outflows is not along the rotational axis, but slightly off-axis. This is because the ram pressures just along the rotational axis, free from the centrifugal forces, are highest, and thus the magnetic pressures cannot overwhelm the ram pressure there. Following these magnetic outflows from the disk, the MHD jets are formed in the two ways (namely type I or II), which we will explain from the next section.

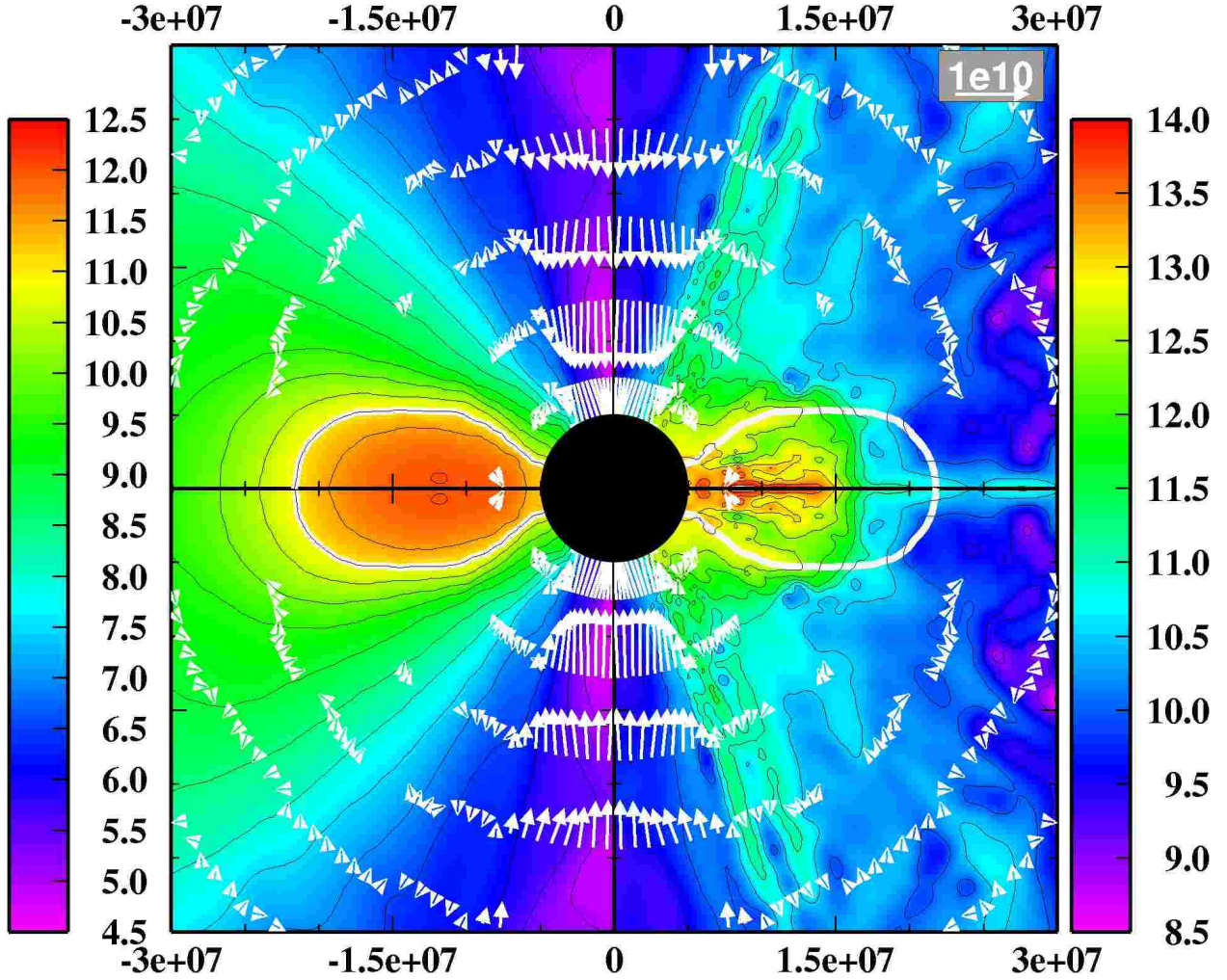


Fig. 2.— Logarithmic contour of density (left) and poloidal magnetic field (right) for B9J1.5 model, just before launching an outflow at 7.99 s. The white solid line (right) denotes the area where the density is equal to 10^{11} g/cm^3 , showing the surface of the accretion disk. The strong poloidal fields inside the accretion disk in the vicinity of the equatorial plane (right) coincide with the high density regions (left). This means that the poloidal fields are amplified mainly by compression. Note that the velocity fields are drawn by the white arrows, and the length is normalized by the scale shown in top right edge of the box (here, $10^{10} \text{ cm s}^{-1}$). The central black circle (50 km in radius) represents the inner boundary of our computations. In the following figures, density line, velocity field, and the inner boundary are depicted in the same manner.

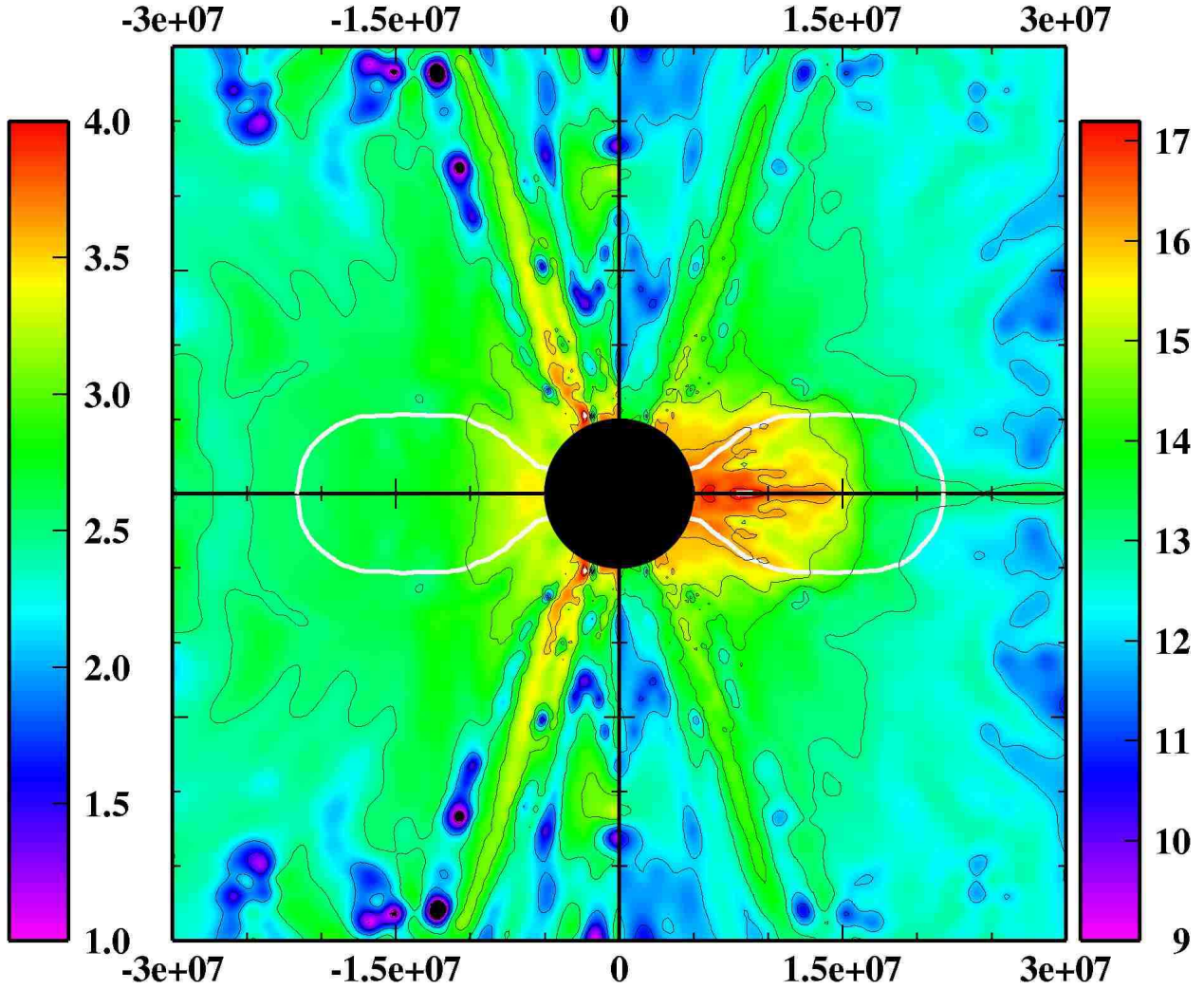


Fig. 3.— Same as Figure 2 but for logarithmic contour of differential rotation ($:Xd\Omega/dX$) (left) and amplification rate of toroidal magnetic field ($:dB_\phi/dt$) (right). Comparing with the right side of Figure 2, the amplification rates become larger where the poloidal fields and the degree of the differential rotation are stronger.

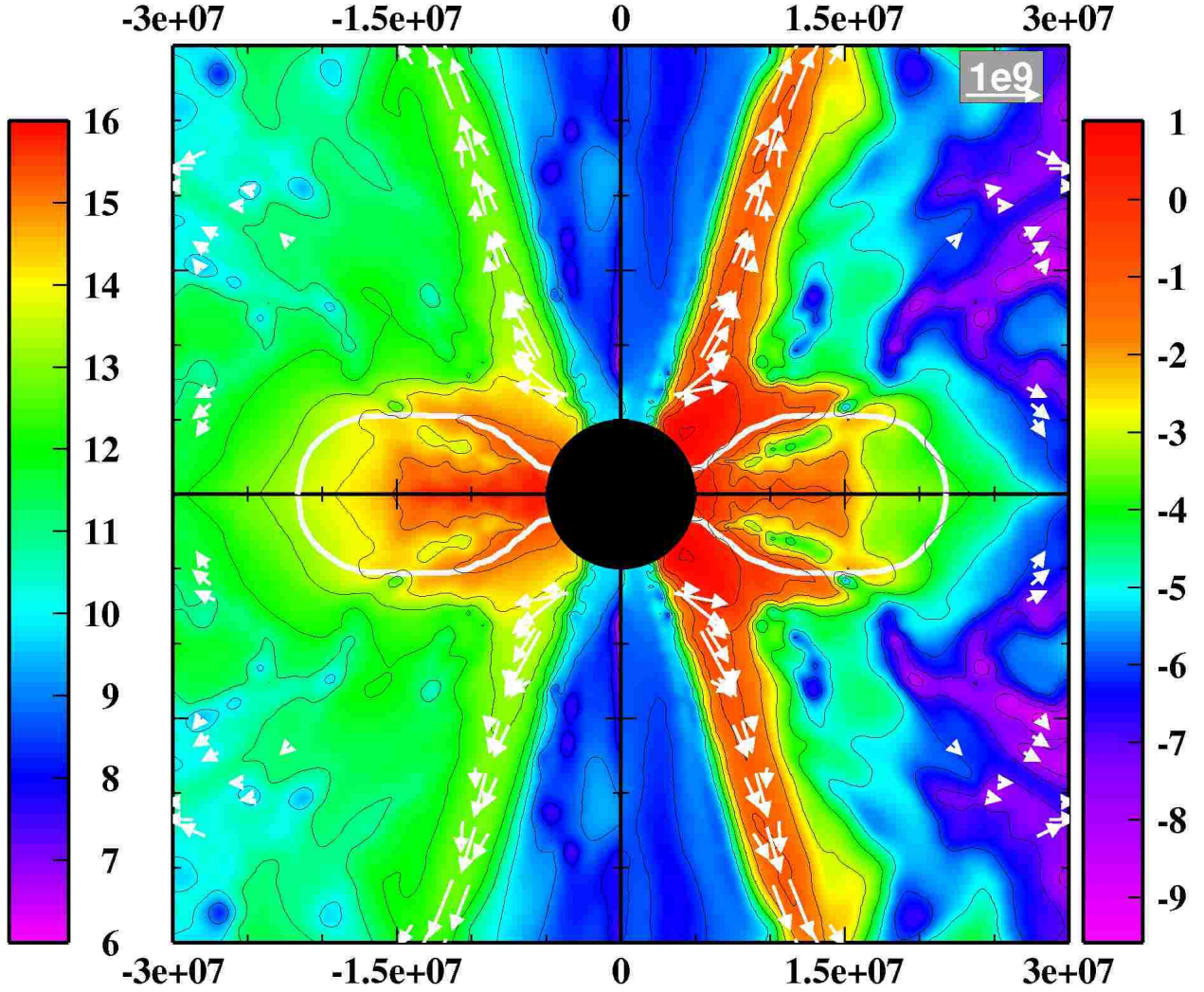


Fig. 4.— Same as Figure 3, but for the logarithmic contour of toroidal magnetic fields (left) and the inverse of plasma beta (e.g., $\beta_{\text{mag}}^{-1} \equiv \mathbf{B} \cdot \mathbf{B}/8\pi/p$) (right). It is shown that the toroidal fields are amplified up to 10^{16} G (left), and that the MHD outflows are driven from the accretion disk (right). In this figure, we plot the velocity fields only for $V_r > 10^8$ cm/s for illuminating the outflows, where V_r is the radial velocity.

4.2.2. Two types of MHD jet formation

When the magnetically-dominated outflows mentioned above are so strong enough to come out of the central iron cores without shock-stall, we call them as type II jets. Even if these prompt outflows stall at first, we find an another way of launching jets (type I), whose formation processes are a little bit complicated than for type II. We first explain type II in the following.

Figure 5 shows the evolution of the MHD outflow for model B10J1.5, from its initiation near from the inner edge of the accretion disk (top left), propagation along the polar axis (top right), till they come out of the iron core (bottom). Note the difference of the length scales in each panel. Among the computed models, this model has the strongest initial magnetic fields with smallest angular momentum (e.g., Table 2). The toroidal fields can be much stronger than for other models, by the enhanced compression of the poloidal fields inside the disk, as mentioned in §4.2.1. As a result, the MHD outflow is so strong that they do not stall, once they are launched. In fact, the outflow is shown to be kept magnetically-dominated (inverse of the plasma beta greater than 1, right-hand side in Figure 5) till the shock break-out. As the disk becomes more compressed, the magnetic pressure of toroidal fields and its vertical gradient inside the accretion disk become larger, which acts to push the outflow vertically more strongly. In the early phase of the jets (top left), the sideway expansion of the outflow is suppressed by the external pressure P_{ext} , which is determined by the ram pressure of a freely falling fluid with velocity of $v_{r_{\text{ext}}}$ as $P_{\text{ext}} \approx \rho v_{r_{\text{ext}}}^2 \approx \rho GM/r_{\text{ext}}$, with r_{ext} being the width of the outflow. r_{ext} is determined by the balance equation of $B^2/8\pi = P_{\text{ext}}$, which gives a reasonable value. This confinement promotes the outflow to keep progressing vertically. As the outflow propagates rather further from the center (top right), the outflow begins to be collimated due to the magnetic hoop stresses, and keep their shape till the shock-breakout (Figure 6). It is interesting to notice that the ram pressure just along the polar axis is so large that no outflow is formed there, and that there stays a polar funnel, where the material accretes onto the central object. We speculate that the formation of the funnel in such an early phase could possibly provide nice environments as a birthplace of fireballs, because the neutrino heating from the disk could be sufficiently high at the epoch as will be discussed in section 5.2.

It should be noted here that the above outflow driven by the toroidal fields is essentially same as the 'magnetic tower' which was first introduced by Lynden-Bell (1996, 2003) in the context of active galactic nucleus, and applied to the collapsar environments (Uzdensky & MacFadyen 2007a,b). However in the analytic models by Uzdensky & MacFadyen (2007a,b), the driven mechanism of the tower are assumed to be the winding of the magnetic fields threaded in the planar accretion disks with no vertical structures inside. Our simula-

tions suggest that the origin comes from the vertical gradient of the twisted toroidal fields inside the accretion disk.

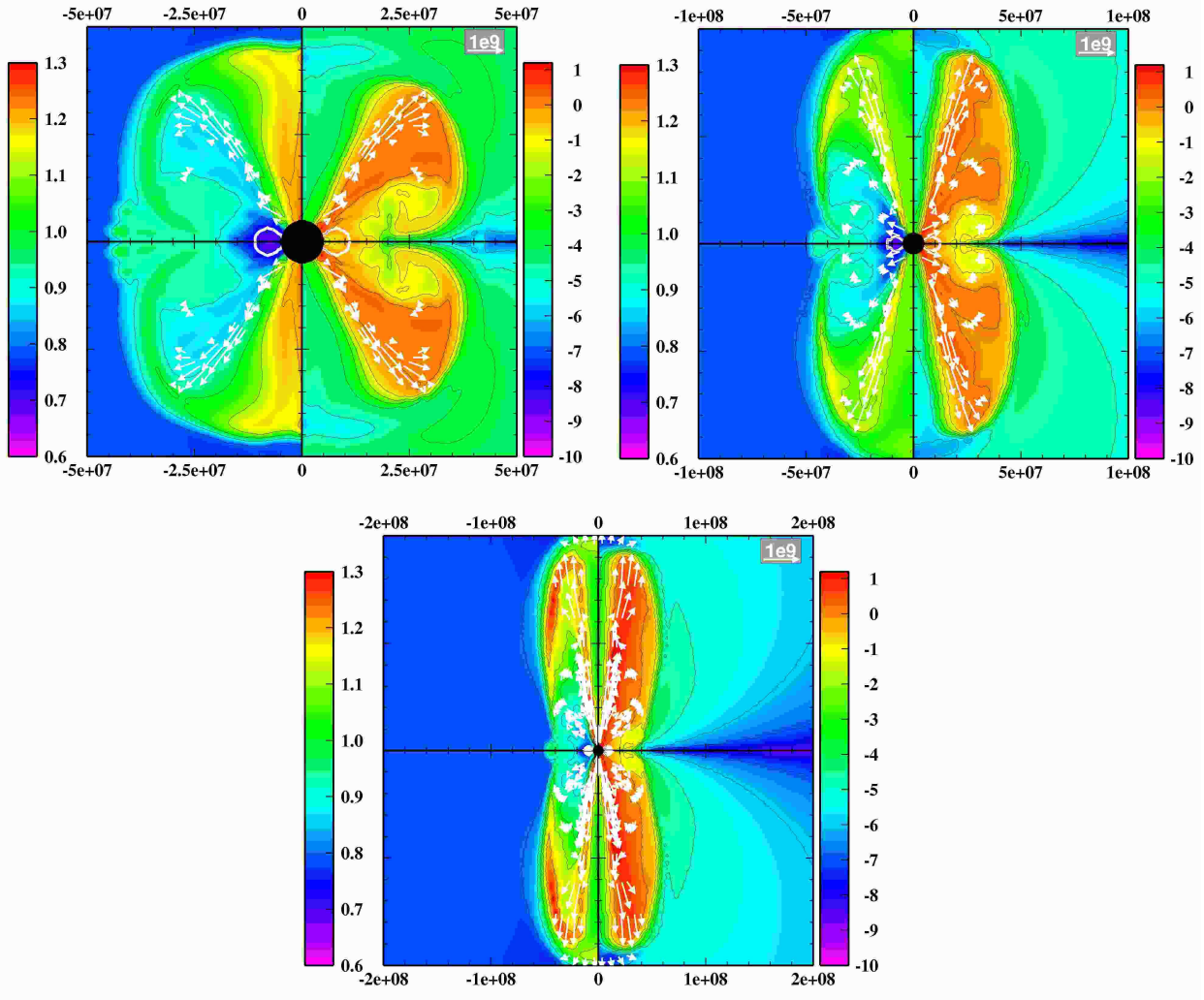


Fig. 5.— Evolution of MHD jets launched from the accretion disk (Type II jets). In each panel, logarithmic contour of entropy (left side) and the inverse of plasma beta (e.g., $\beta_{\text{mag}}^{-1} \equiv \mathbf{B} \cdot \mathbf{B} / 8\pi / p$) (right side) are shown at 1.43 s (top left), 1.87 s (top right), and 2.11 s (bottom) for model B10J1.5. Note the difference of the length scales among panels. Without shock-stall, magnetically-driven outflows ($\beta_{\text{mag}}^{-1} \gtrsim 1$) come out of the iron core (~ 3000 km in radius).

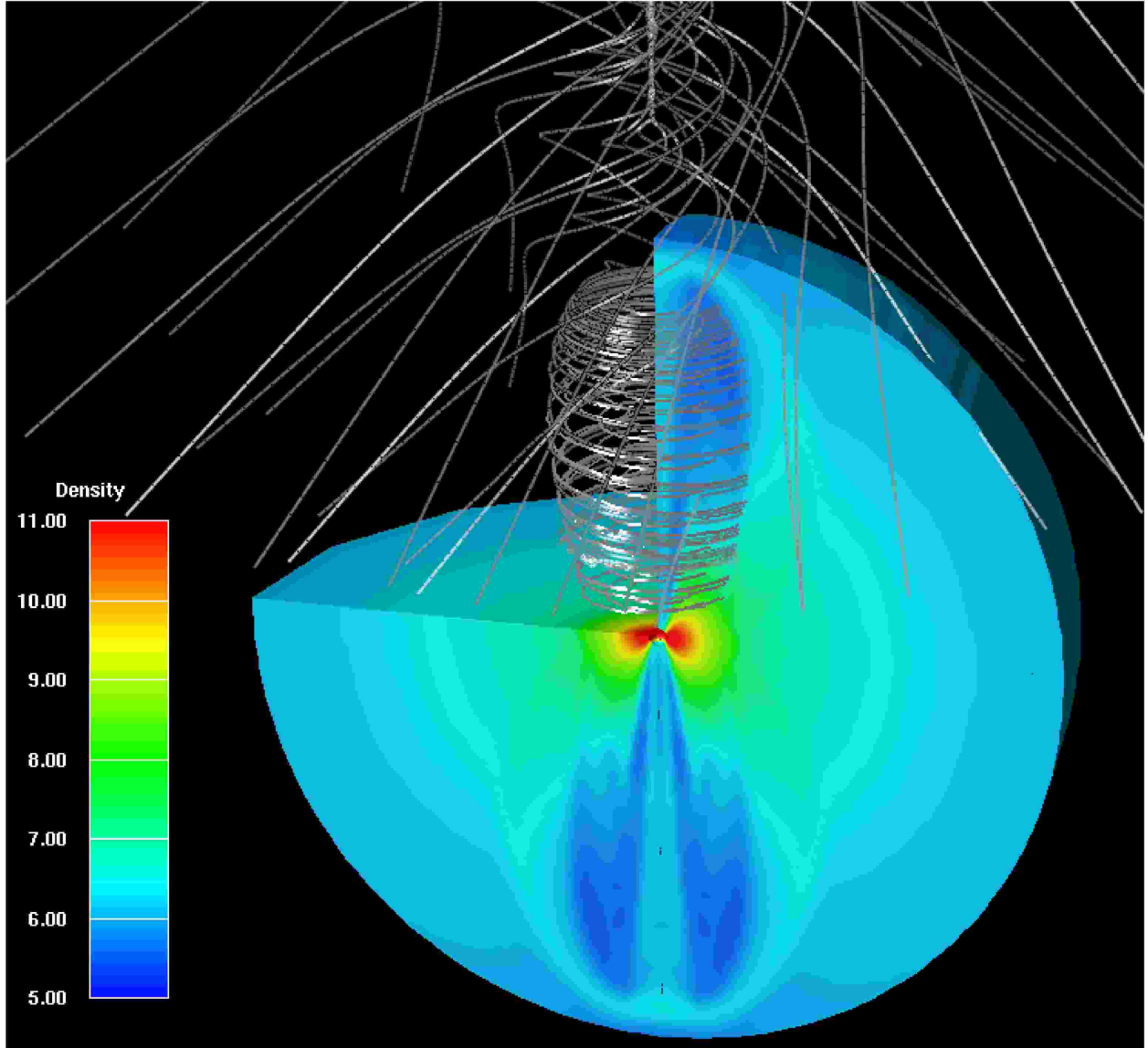


Fig. 6.— Three dimensional plot of density with the magnetic field lines (silver line) for B10J1.5 model near at the moment of the shock break-out (2.11 s). Color contour on the two-dimensional slice represents the logarithmic density. The outer edge of the sphere colored by blue represents the radius of 2×10^8 cm. The outflow is shown to be driven by the so-called magnetic tower, i.e., by the toroidal fields tangled around the rotational axis. Note that the field lines outside the bluish region, seen to be more weakly twisted than inside, come mainly from the preshock region.

Now we move on to discuss the jets in type I, by taking model B9J1.5 as an example. In this case, the magnetic outflow from the accretion disk is not as strong as model B10J1.5, and stalls at first in the iron core (see butterfly-like regions colored by red in the top left panel (right-hand side) in Figure 7). In the top right panel, very narrow regions near along the rotational axis are seen to be produced in which the magnetic pressure dominate over the matter pressure (colored by red in the right-hand side). Such regions are formed by turbulent inflows of the accreting material from the equator, crossing the butterfly-like regions outside the disk, to the polar regions. Such flow-in materials obtain sufficient magnetic amplifications when they approach to the rotational axis where the differential rotation is stronger, leading to the formations of the MHD outflows along the rotational axis (bottom).

Figure 8 shows the magnetic pressure of the toroidal fields and the ram pressure of the accreting material near along the rotational axis for the same time epoch as in Figure 7. The mentioned turbulent inflows to the polar regions happens at 8.148 s (top right), showing the increase of the magnetic pressure in the central region within 100 km. When the toroidal fields are amplified enough to overwhelm the local ram pressure, ρv_r^2 with v_r being the radial velocity (bottom), the flow-in materials begin to move outwards (bottom in Figure 7). In fact, at about 70 ms later, the initiated outflows can produce the well-collimated magneto-driven explosions, reaching ~ 1000 km along the polar axis (Figure 9). Although the shape of the narrow jets are much like the ones obtained in previous collapsar simulations with much rapid rotation and strong magnetic fields (e.g., Fujimoto et al. (2006)) or with slower rotation (e.g., Proga (2005); Mościbrodzka & Proga (2009)), it should be noted that their formation processes are different. The obtained outflow here is peculiar as a consequence of the long-term evolution of collapsars, which is produced by the interplay between the decreasing ram pressure and the magnetic twisting of the turbulent inflow in the vicinity of the polar region.

Now let us return to Table 2 again. Among the models with outflows, models B10J1.5 and B10J2.0 make the type II jets, and the other make the type I jets. As mentioned, the type II is obtained for models with stronger magnetic fields with relatively smaller angular momentum. If each of these conditions were not satisfied, the MHD outflows would stall at one time but with the subsequent revival (type I) or stall forever (\times in Table 2).

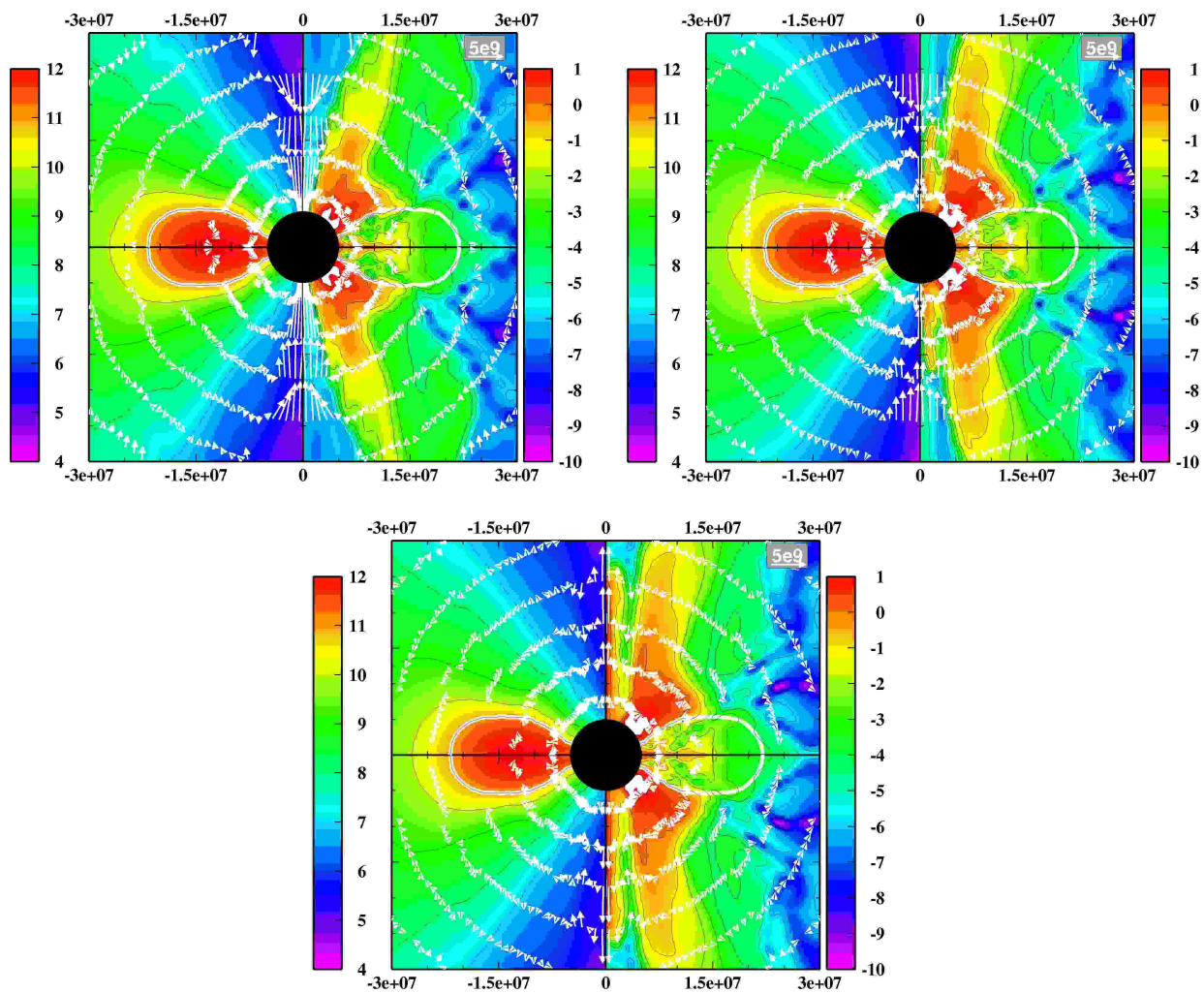


Fig. 7.— Same as Figure 4 but for model B9J1.5 at 8.115 s (top left), 8.148 s (top right), and 8.154 s (bottom), showing the moment of the formations of jets in type I. In the top right panel, very narrow magneto-driven regions along the rotational axis are produced by inflows of the accreting material in the equator to the polar regions. Such flow-in materials are shown to start propagating along the rotational axis (bottom).

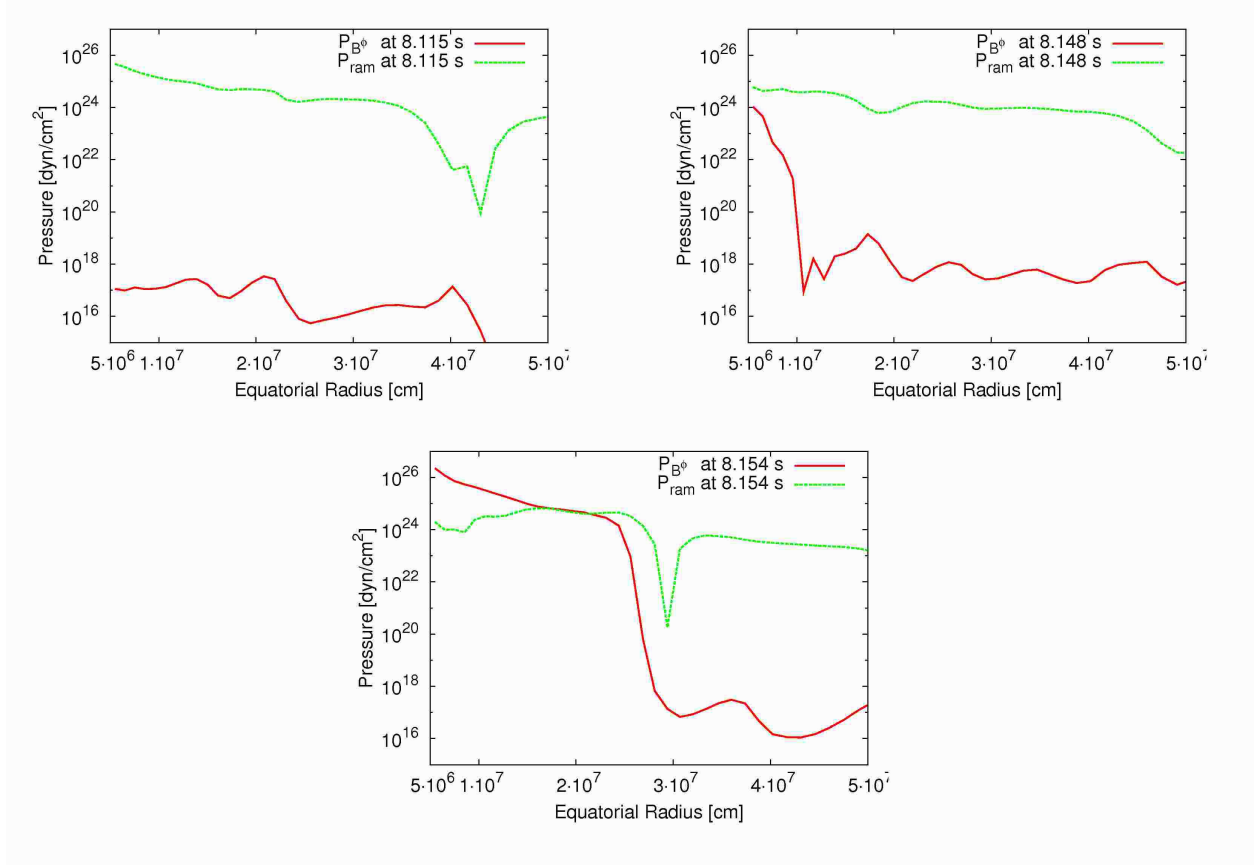


Fig. 8.— The magnetic pressure of toroidal fields vs. the ram pressure for model B9J1.5 at 8.115 s (top left), 8.148 s (top right), and 8.154 s (bottom) along the rotational axis, respectively. Note that the timescales correspond to the ones in Figure 7. Only after the magnetic pressure becomes dominant over the ram pressure (bottom), the materials inside ~ 200 km begin to propagate outwards.

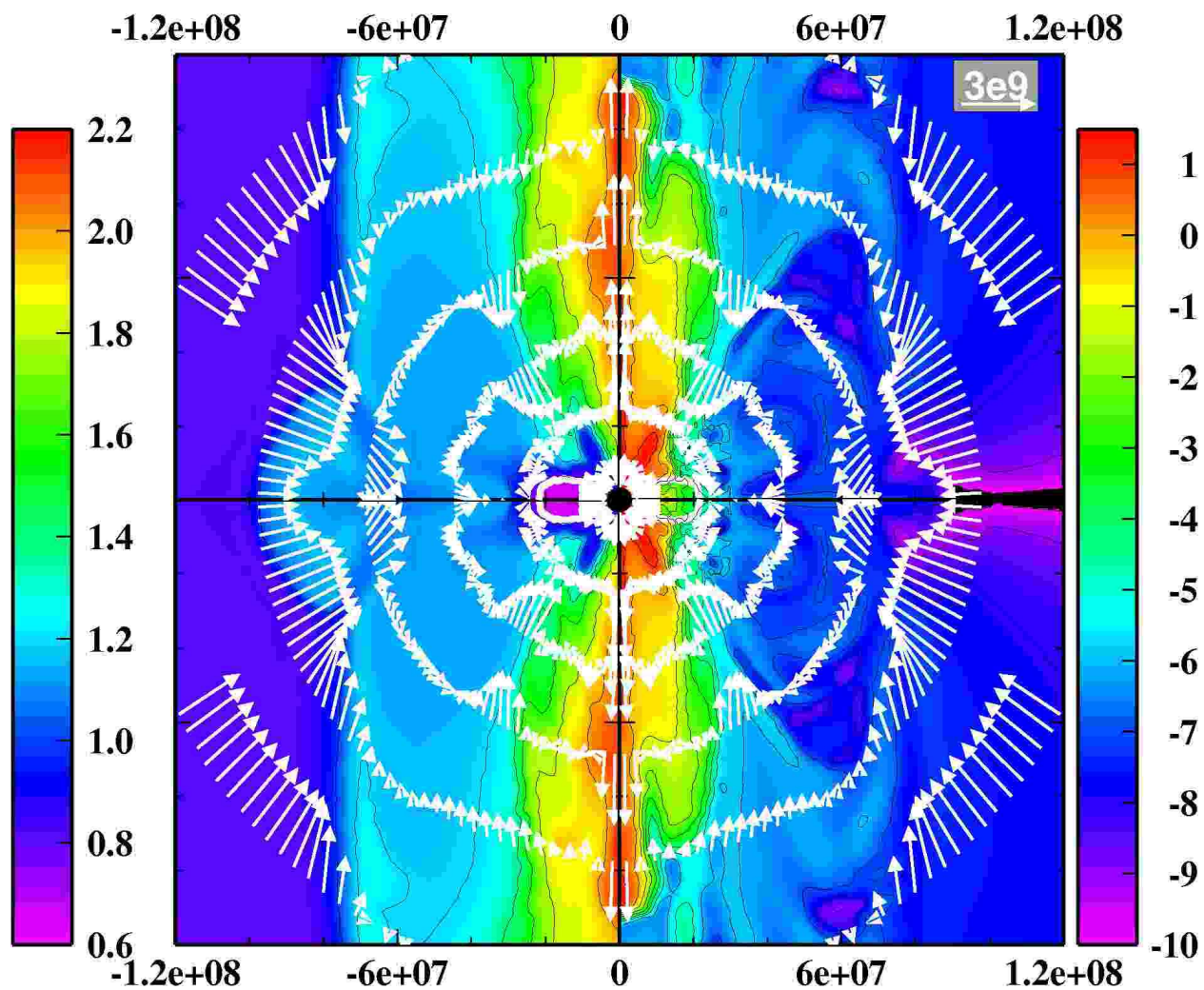


Fig. 9.— Logarithmic contour of entropy (left) and inverse of plasma beta (right) for B9J1.5 model at 8.23 s. The narrow magneto-driven explosions are shown near the rotational axis, which is produced by the type I mechanism (see text). High entropy region (~ 20) outside the collimated jets (colored by light-blue (left)) is a cocoon, which is produced by a fallback of the matter from the shock front.

| Model | $t_{\text{jet}} [s]$ | $M_{\text{jet}} [M_{\odot}]$ | $E_{\text{jet}} [\text{erg}]$ | Γ_{jet} | $\Gamma_{\text{jet,mag}}$ |
|---------|----------------------|------------------------------|-------------------------------|-----------------------|---------------------------|
| B10J1.5 | 2.66 | 1.3×10^{-3} | 5.6×10^{48} | 1.0024(0.07c) | 1.043(0.28c) |
| B10J2.0 | 3.80 | 5.1×10^{-4} | 5.5×10^{47} | 1.00063(0.04c) | 1.0087(0.13c) |
| B10J2.5 | 6.33 | 9.3×10^{-4} | 6.5×10^{47} | 1.0021(0.06c) | 1.052(0.31c) |
| B10J3.0 | 8.89 | 1.7×10^{-4} | 2.4×10^{47} | 1.0077(0.04c) | 1.031(0.24c) |

Table 3: Properties of MHD Jets. t_{jet} is the time when the jets come out of the iron core. M_{jet} and E_{jet} is the mass and the explosion energy of jets, respectively. Γ_{jet} and $\Gamma_{\text{jet,mag}}$ represent the Lorentz factors (and the velocity normalized by the speed of light) and their maximum values estimated by taking into account the magnetic energies, respectively. Note that all of them are estimated at t_{jet} .

4.2.3. Properties of MHD jets

Now we proceed to look more in detail to the properties of the MHD jets. Here we focus on the models with B10, because all the model sequence is accompanied with the jets either type I or II (Table 2).

Table 3 shows the mass, explosion energy, and Lorentz factor of jets at the moment of shock break-out. Here it is noted that the explosion energy is estimated for the regions where the local energy is positive and the radial velocity is positive, indicating that the matter is not bound by the gravity (see the definition of $e_{\text{local}} > 0$ in Appendix A). As seen in the table, the jet of model B10J1.5 has the largest explosion energy with largest baryon loading. This is because the jet is type II as mentioned. Since the jet is launched rather earlier (~ 1.9 s) than for type I, there is much material near the rotational axis, which makes the baryon-load of jets larger for the model. For type I jets, no systematic dependence of the initial angular momentum on the masses and the energies is found. We think that this is because the formation of the type I jets occurs by turbulent inflows as already mentioned in the previous section.

The similarity between types I and II is that the jets are at most subrelativistic (0.07c for model B10J1.5) with the explosion energy less than 10^{49} erg. To see the maxim of the Lorentz factor in our computations, we boldly assume that the magnetic energy of the fluid is fully converted to the kinetic energy, having in mind the dissipative process such as magnetic-reconnection ($\Gamma_{\text{jet,mag}}$ in Table 3). Even in this case, the jets become only mildly relativistic. While the ordinary GRBs require the highly relativistic ejecta, we speculate that these mildly relativistic ejecta may be favorable for X-ray flashes (Soderberg et al. 2006; Ghisellini et al. 2007), which is a low energy analogue of the GRBs. The propagation of the MHD jets can

expel the matter along the polar axis. Such baryon-poor environments may be a favorable site for producing the subsequent jets, which could attain high Lorentz factors pushed by the magnetic outflows and/or heated by neutrinos. From the next section, we study the properties of neutrino luminosities obtained in our simulations and discuss how the neutrino heating, albeit not coupled to the hydrodynamics here for simplicity, could have impacts on the jet formations.

4.3. Properties of neutrino luminosity

As seen in Figure 1 (left), the disk masses for models with the MHD jets ($j \geq 1.5j_{\text{iso}}$), differ several times at most. On the other hand, the neutrino luminosities, which are contributed mainly from the accretion disk, differ up to 3 orders-of-magnitudes (Table 2). This indicates that the local neutrino emissivities also change over several orders-of-magnitudes in the vicinity of the disk. In this section, by focusing on the structures of the disk, we discuss how the properties of the neutrino luminosities change for the models with different initial angular momentum.

By comparing Figures 10 with 11, it can be seen that for smaller initial angular momentum (Figure 10), the disk becomes more compact (top left) with higher temperatures (top right), and that the resulting enhancement of the electron captures lower Y_e in the disk (bottom). The enhanced compression is a primary reason for the higher neutrino luminosities for slower rotating models in Table 2.

The left panel of Figure 12 shows that the disk, whose equatorial size is $\sim 200\text{km}$ (top left in Figure 10), is very thick to neutrinos. In fact, the opacity inside the disk becomes up to 200 for ν_e inside the disk, which is one order-of-magnitude larger than that for $\bar{\nu}_e$. The right panel shows that the local neutrino emissivities are highly suppressed by $\exp(-\tau_\nu)$ with τ_ν being the opacity, which gives the actual neutrino cooling rates in such a thick region (dashed lines). The higher suppression for ν_e makes its cooling rate almost comparable to that of $\bar{\nu}_e$, which is also shown in Figure 13. It is noted that because of this high neutrino opacity inside the disk, the characteristic neutrino cooling timescale is typically more than four orders-of-magnitudes longer than the advection timescale. Thus the disk of our models is advection dominated flow.

Figure 14 shows the evolution of neutrino luminosities for each neutrino species (ν_e (top left), $\bar{\nu}_e$ (top right), and ν_X (bottom)). It is shown that for every species, the luminosities become larger for models with smaller angular momentum due to the mentioned higher compression, and also that the luminosities of ν_e and $\bar{\nu}_e$ are dominant over the ones of ν_X . For models with J1.5 and J2.0, the luminosities of $\bar{\nu}_e$ become almost comparable to those of ν_e , while the luminosities of $\bar{\nu}_e$ are much smaller than those of ν_e for more rapidly rotating models (compare top left and right panels in Figure 14 noting the difference of the vertical scales). On top of the effect of opacity mentioned above, this is because the higher compression leads to the production of positrons more abundantly, which promotes the production of $\bar{\nu}_e$ via the positron captures.

Figure 14 also depicts the effect of the magnetic fields on the luminosities (compare between B8J1.5, B9J1.5, and B10J1.5). For every neutrino species, the luminosities are

shown to become smaller for models with larger initial magnetic fields. For stronger magnetized models, the disks expand more due to the magnetic pressure inside, leading to the suppression of the contraction.

Among the computed models, the total neutrino luminosity becomes largest $\sim 10^{52}$ erg/s for model with J1.5 series (e.g., Table 2). It is well known that the energy deposition rate via pair neutrino annihilation ($\nu + \bar{\nu} \rightarrow e^- + e^+$) is proportional to $L_\nu \cdot L_{\bar{\nu}}$ with being the neutrino and anti-neutrino luminosities, respectively (Salmonson & Wilson 1999; Asano & Fukuyama 2001, 2000). Thus almost the equivalent luminosities of ν_e and $\bar{\nu}_e$ is advantageous for making the deposition rate larger for a given sum of the luminosities. Due to the two factors, the models with smallest angular momentum computed here are expected to be most suitable for making the fireballs via neutrinos.

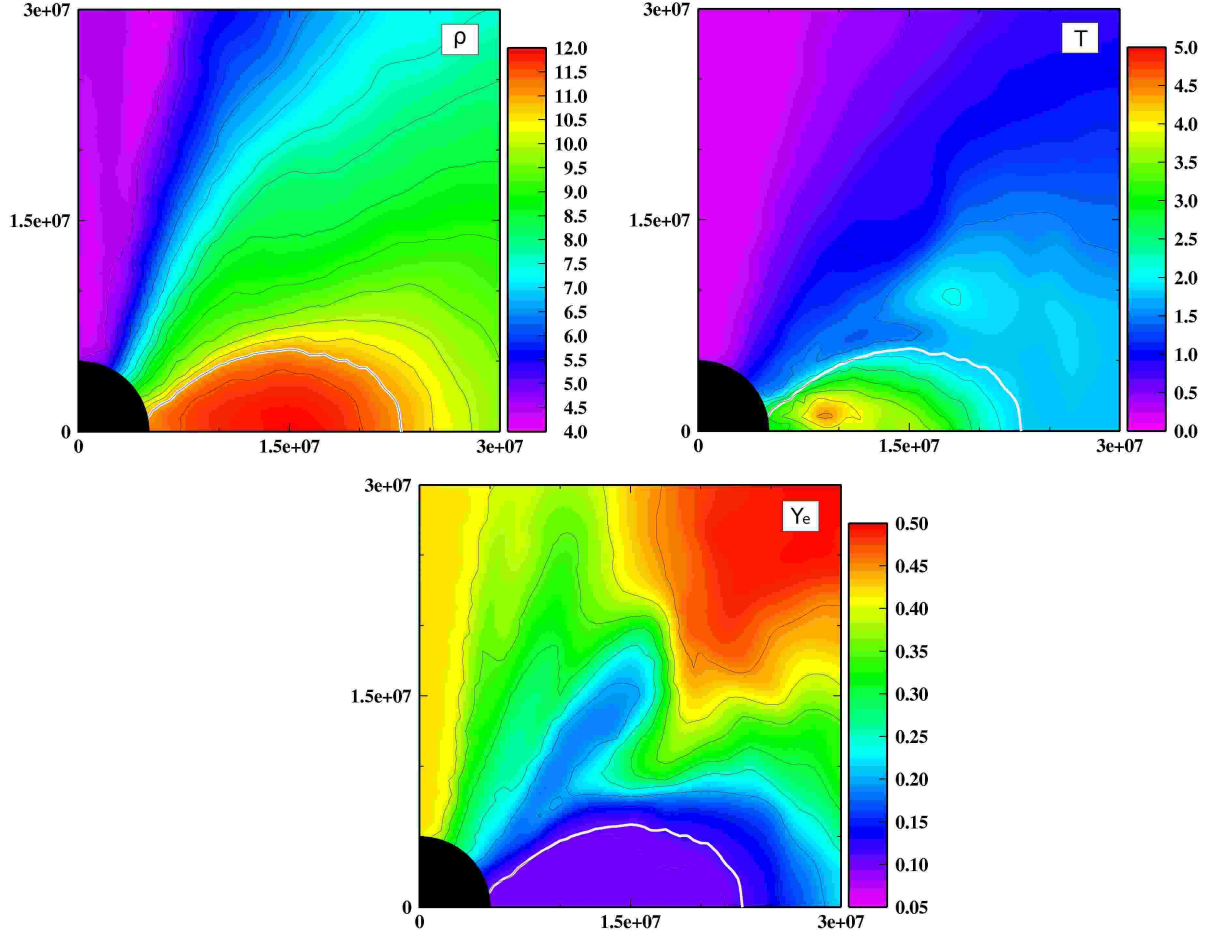


Fig. 10.— Contour of density [g/cm^3](top left), temperature [MeV](top right), and electron fraction (bottom) for model B9J1.5. These panels are for 9.22 s, when the accretion disk becomes stationary (see left panel of Figure 1). The white line marks $\rho = 10^{11} \text{ g/cm}^3$, representing the surface of the disk. Comparing with Figure 11 which has larger angular momentum initially, it can be seen that the disk here is more compact (top left) with higher temperatures (top right), and that the resulting enhancement of the electron captures lowers Y_e in the disk (bottom).

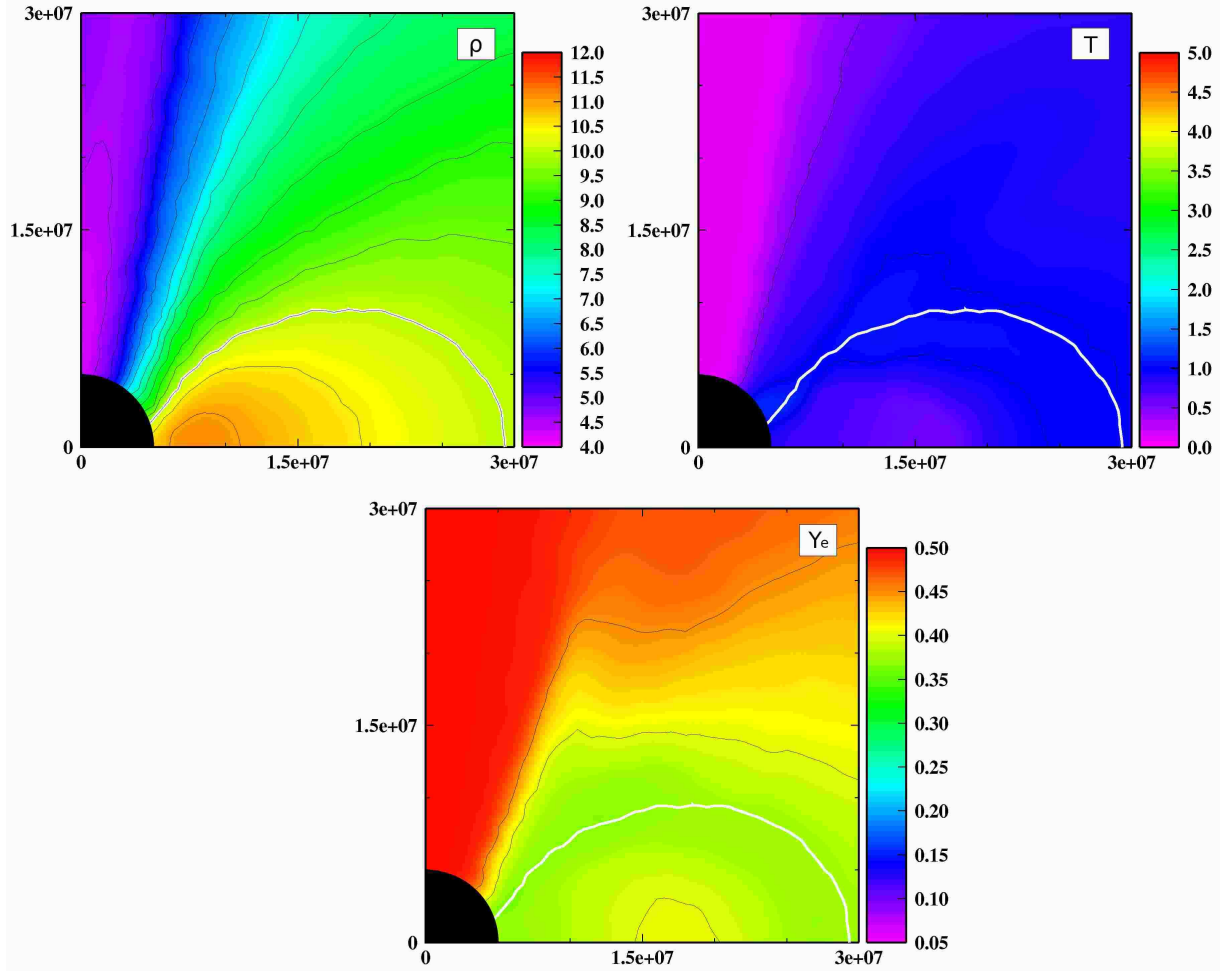


Fig. 11.— Same as Figure 10 but for model B9J3.0. Note here that the white line marks $\rho = 10^{10} \text{ g/cm}^3$.

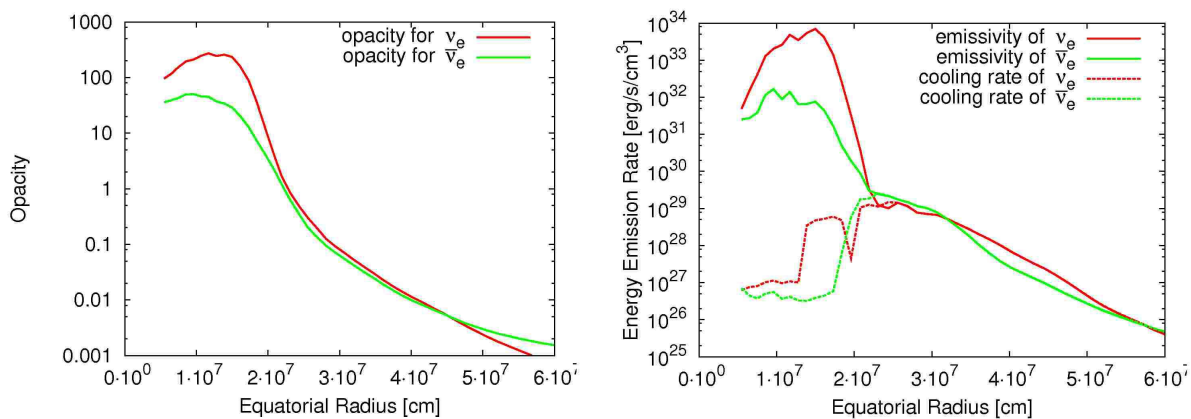


Fig. 12.— Plots of opacity (left), emissivity (solid line, right), and cooling rate (dashed line, right) for ν_e (red) and $\bar{\nu}_e$ (green) along the equatorial plane of model B9J1.5 at 9.22 s. The cooling rates are greatly reduced from the local neutrino emissivities for the opaque regions ($\lesssim 200$ km). For such regions, the higher suppression for ν_e makes its cooling rate almost comparable to that of $\bar{\nu}_e$.

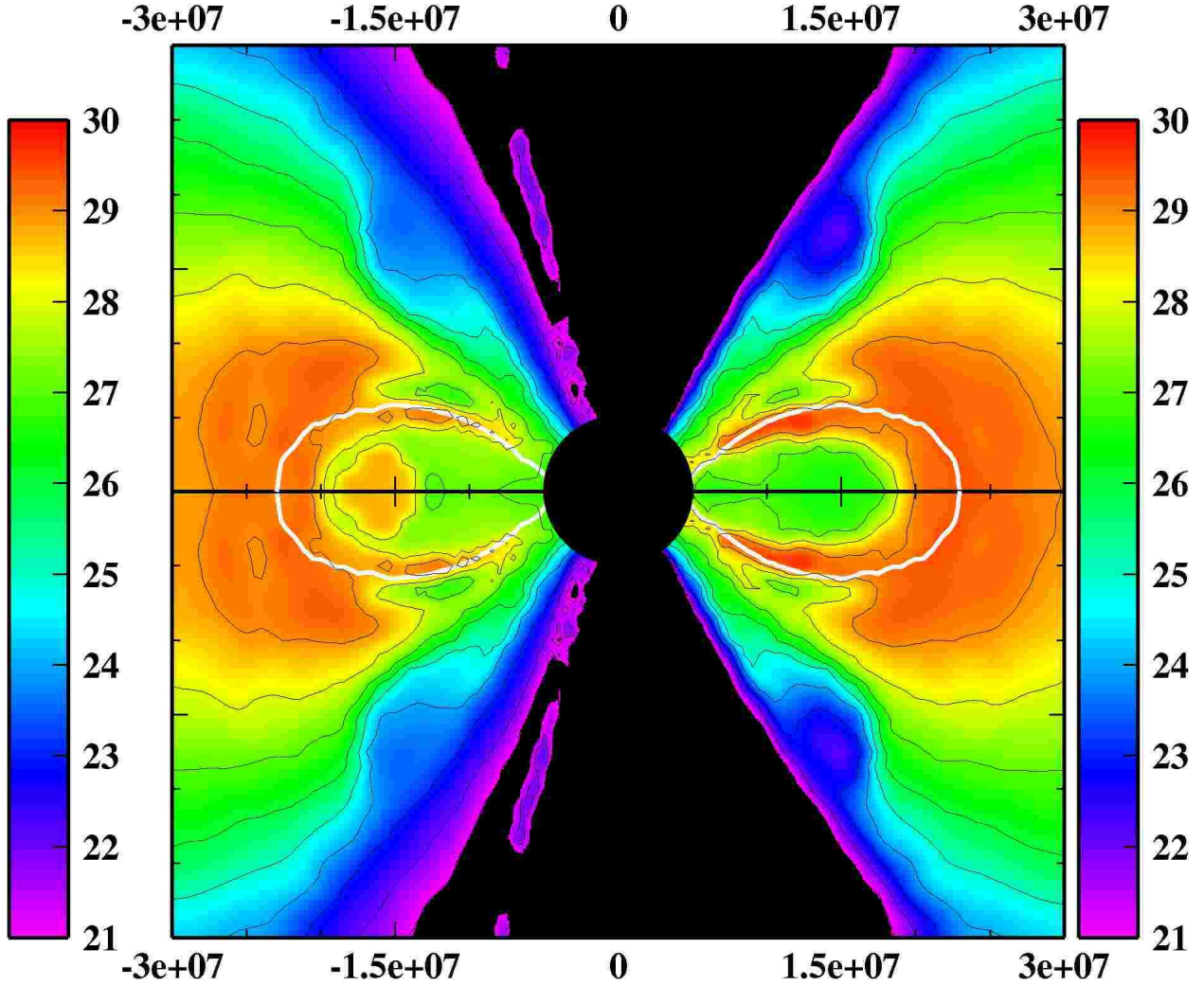


Fig. 13.— Logarithmic contour of the cooling rates for ν_e (left), and for $\bar{\nu}_e$ (right) for model B9J1.5 model at 9.22 s. It is shown that the luminosities of ν_e and $\bar{\nu}_e$ are almost comparable. Regions colored by black have lower values than the limit of the color legend, which is out of our interest here. The white line marks $\rho = 10^{11} \text{ g/cm}^3$, indicating the surface of the disk.

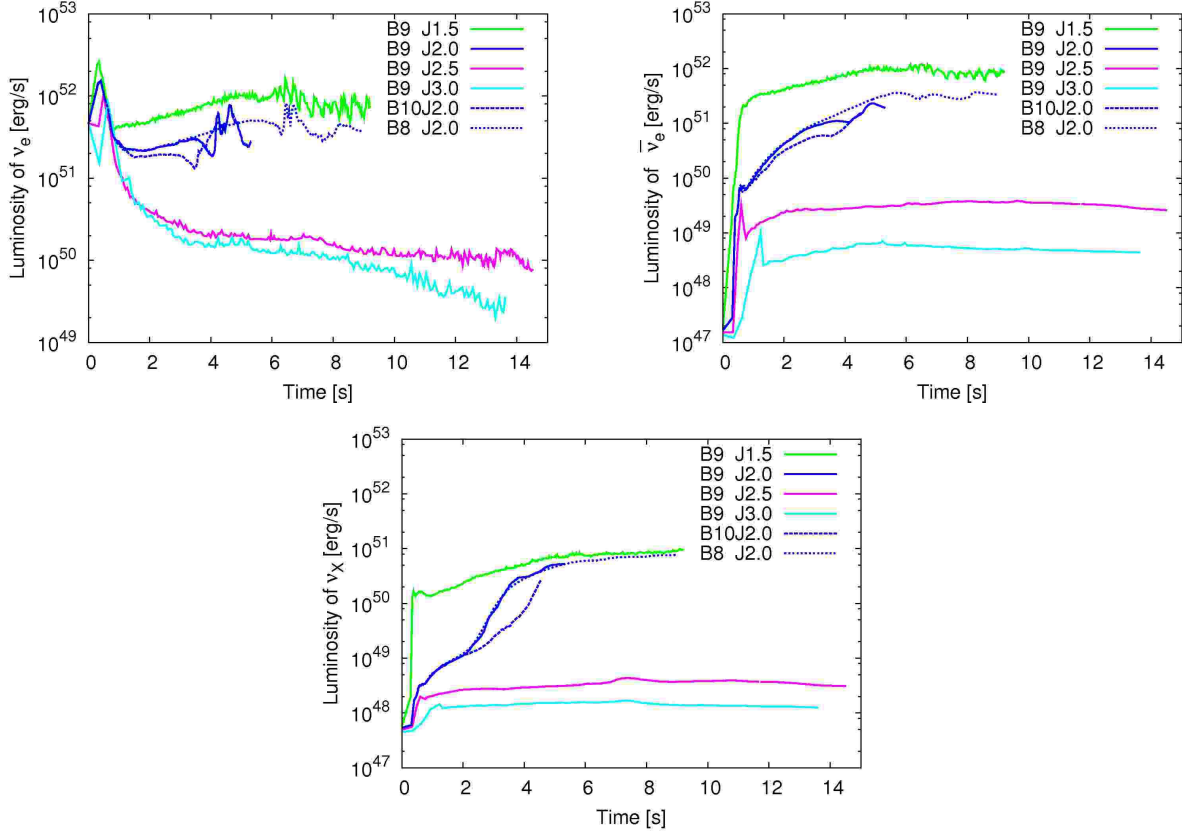


Fig. 14.— Plots of time evolution of the luminosity for ν_e (top left), for $\bar{\nu}_e$ (top right), and for ν_X (bottom). For slower models with J1.5 and J2.0, the neutrino luminosities of ν_e and $\bar{\nu}_e$ become almost comparable, which is expected to be advantageous for energetizing the jets via neutrino heating.

5. Discussion

Here we shall discuss limitations of our simulations and requirements towards more sophisticated numerical modeling of collapsar, such as the effects of inner boundary (section 5.1), the effects of neutrino heating (section 5.2), and the importance of general relativity (section 5.3). The latter two is neglected or treated by a simple approximation in this paper. Numerical tests are given in section 5.4.

5.1. Effects of inner boundary

First of all, we discuss possible drawbacks due to the large inner boundary (50 km) taken in this simulation. For the Schwarzschild metric, the marginal stable orbit can exist for $j > 2r_g c$ where r_g is the gravitational radius. Such orbiting flow can lead to the formation of the shock on the equatorial plane, and is predicted to result in the formation of stable and thick disk as shown in Proga et al. (2003a); Proga (2003); Lopez-Camara et al. (2009). To capture such a feature needs the inner boundary as small as $R_{\text{in}} > 2r_g$. However, our inner boundary is larger than the value. For example, models B10J1.5 and B9J1.5 have the central object with mass of $2.5M_\odot$ and $3.5M_\odot$ at the end of computation, which corresponds to $r_g = 7.5\text{km}, 10.5\text{km}$, respectively. Our inner boundary corresponds to $6.7r_g, 4.8r_g$ for each model. Therefore the critical angular momentum to form the stable accretion disk discussed in this paper could be affected by the position of the inner boundary. Moreover the large inner boundary, which excises the inner edge of the accretion disk, should lead to the underestimation of the neutrino luminosity and the resulting neutrino heating, which we will discuss in the next section. To clarify those points, we are now planning to implement more compact inner boundary in the long-term evolution, which is computationally very demanding, thus as a sequel of this paper.

5.2. Importance of Neutrino Heating

We try to estimate the effects of the neutrino energy deposition via neutrino pair annihilation ($\nu + \bar{\nu} \rightarrow e^- + e^+$) from the accretion disk to the polar funnel. The neutrino heating is important, however, not included in the simulations here for simplicity.

In the following, we present an order-of-magnitude estimation of the heating rate. To do so, we derive the heating rate with the special relativistic corrections (see Appendix C). For simplicity, we take the so-called optically thin limit in the accretion disk as in Asano & Fukuyama (2001) and consider the neutrino heating only along the rotational axis. It is noted that ex-

pect for the polar funnel, to make neutrino-heated outflows is hopeless due to the baryon contamination. By comparing timescales such as heating and advection, we discuss how important the heating could be.

Figure 15 shows various timescales. $\tau_{\text{rel}} \equiv \rho c^2/q^+$ characterises the timescale for matter to become relativistic by the neutrino heating, in which ρ and q^+ represent the local density and the heating rate, $\tau_{\text{rel}} \equiv \rho c^2/q^+$ is the timescale when the motion of the matter becomes relativistic due to the energy deposition, $\tau_{\text{int}} \equiv e_{\text{int}}/q^+$ is the timescale when the neutrino heating is comparable to the internal energy (e_{int}) and thus affects the dynamics, $\tau_{\text{hyd}} \equiv X/|v_r|$ indicates the hydrodynamical timescale with X and v_r being the length and radial velocity along the polar axis, $\tau_{\text{light}} \equiv X/c$ is the light crossing timescale. As shown, τ_{int} gets shorter to be several milliseconds near around 100 km, where the timescales become most close to τ_{hyd} . This means that rather in the vicinity of the center ($\lesssim 200$ km along the rotational axis), the neutrino heating have potential importance to affect the hydrodynamics. However, it should be noted that it does not directly mean that the heated matter could become relativistic. In fact, τ_{rel} is at least two orders-of-magnitudes larger than τ_{light} .

For making the outflows relativistic, one possible way is to decrease τ_{rel} by lowering the density of the funnel regions. Such low density regions would be formed if we continue to follow the dynamics of collapsar in more longer term. Unfortunately however, the numerical difficulty of treating such force-free fields prevents us from doing so. The numerical code specially developed to solve the force-free fields is required (e.g., McKinney (2006)), which is major undertaking. Another way is to increase the heating rate q^+ . If the neutrino heating not just from the equatorial plane here but also from the whole accretion disk could be included such as by the ray-tracing calculation (Birkel et al. 2007), the deposition rates would become larger due to the geometrical effects. Dissipative processes such as magnetic-reconnection/Joule heating (e.g., Proga et al. (2003a)) inside the disk would rise the temperature, which could be also good for achieving the higher luminosity. Furthermore, general relativistic effects would increase the deposition rate in the vicinity of the BH (Salmonson & Wilson (1999); Asano & Fukuyama (2001, 2000)), which is also remained to be studied.

5.3. General relativistic effects

As mentioned earlier, we have employed the Paczynsky-Wiita potential to mimic the Schwarzschild metric. With the special relativistic modification, this artificial potential is known to be able to approximate the general relativistic (GR) motion well for the regions $r > 3r_g$ (with r_g being the Schwarzschild radius, e.g., Abramowicz et al. (1996), Fukue (2004)), to

which we focused on in this study. However needless to say, what is needed for collapsars is GR simulations around the Kerr BH (e.g., Shibata et al. (2007); Montero et al. (2008) and see discussions in Woosley & Heger (2006)).

The maximum mass of neutron stars, depending on nuclear equations of state, is estimated to be less than typically $3.0M_{\odot}$ (Lattimer & Prakash 2001; Zhang et al. 2008). Following this criteria, the central objects of models with smaller initial angular momenta of J1.0 and J1.5 may collapse into the BHs near within 3 s (Figure 1 (left)). In such cases, GR effects very close to the inner edge of the accretion disk should be important and their impacts on the MHD outflows and the neutrino heating should be investigated. It is naturally expected that strong gravity due to GR effects will lead to not only the efficient gravitational-wave emission, but also the enhanced neutrino emission due to the compression. As recently studied extensively in the context of core-collapse supernovae (e.g., Kotake et al. (2009); Kawagoe et al. (2009); Ott (2009) and references therein), gravitational-wave and neutrino signatures also from collapsars should give us a new observational window to probe the central engine. This paper is a prelude before our forthcoming work to clarify those aspects, which will be presented elsewhere soon.

5.4. Numerical Tests

Figures 16 and 17 show a convergence of our numerical results for different grid resolutions. Figure 16 shows an agreement of the neutrino luminosity. This means that the evolution of the accretion disk, whose temperature and density profiles determine the neutrino luminosity, is numerically converged for the different resolution we tested. On the other hand, Figure 17 shows that the magnetic energies before ~ 3 sec are rather sensitive to the numerical resolution, although the overall trends are similar. We suspect that the discrepancy in the earlier phase should come mainly from the effects of MRI, which are difficult to be captured by our numerical resolution as already mentioned in 4.2.1.

Then we discuss the validity of the equatorial symmetry assumed in this study. Figure 18 shows that the obtained luminosities agree well with each other, however the magnetic energy differs up to two times (Figure 19). This could be also due to MRI. As mentioned, our numerical resolutions can treat MRI marginally in the sense that it can follow MRI in the late phase when the field strength becomes stronger, while it cannot resolve MRI sufficiently in the early phase when the field strength is weaker. In this sense, the obtained results should give a lower bound for the criterion of the field amplification and the jet formation. To capture MRI fully is unquestionably important for collapsar simulations, but possibly needs the prescription such as by the adaptive mesh refinement scheme (e.g., Zhang & MacFadyen

(2009)), which we pose as a future task.

6. Summary

In light of the collapsar model of gamma-ray bursts (GRBs), we presented our numerical results of two-dimensional magnetohydrodynamic (MHD) simulations of the collapse of rotating massive stars. Pushed by recent evolution calculations of GRB progenitors, we focused on lower angular momentum of the central core than previously assumed. As for the initial magnetic field strength, we chose to explore relatively smaller field strength ($\lesssim 10^{10}$ G), which has been less investigated so far. By performing special relativistic simulations including both realistic equation of state and neutrino cooling, we followed a long-term evolution of the slowly rotating collapsars up to ~ 10 s. Then we studied how the formation of MHD jets and the properties of accretion disks could change with the initial angular momentum and the initial magnetic field strength. The obtained results can be summarized as follows.

1. Our numerical results show that for the GRB progenitors to function as collapsars, there is a critical initial angular momentum: $j_{\text{crit}} = 1.5j_{\text{lso}}$ with j_{lso} being the angular momentum of the last stable orbit, below which matter is quickly swallowed to the central objects, no accretion disks and no MHD outflows are formed.
2. When larger than the criteria, we find that smaller initial angular momentum leads to more compact accretion disk due to compression. It seemed widely to be agreed in previous collapsar simulations that the differential rotation is a primary agent to amplify the toroidal fields and the resulting MHD outflows. On the other hand, our results show that for relatively slow rotation models, the amplification of the poloidal fields by compression is preconditioned for the amplification of the toroidal fields and the MHD outflows.
3. Among the computed models, we find the launch of the MHD jets in the following two ways. For models with stronger initial magnetic fields ($B_0 \gtrsim 10^{10}$ G), the gradient of the magnetic pressure perpendicular to the equatorial plane inside the accretion disk can drive the MHD outflow. This outflow makes the strong magnetic explosions like a 'magnetic tower', which we called as type II. For models with weaker initial magnetic fields, the magnetic tower stalls first and the subsequent MHD outflow is produced by the accreting material from the equator to the polar region. Type I jet is found to be produced when such flow-in materials obtain sufficient magnetic amplifications, due to

the strong differential rotation near the rotational axis, to overwhelm the ram pressure of the accreting material.

4. Regardless of type I or II, the jets can attain only mildly relativistic speeds with the explosion energy less than 10^{49} erg. Such events could possibly be related to the X-ray flashes. After the passage of the MHD jets, the baryon-poor environments will be left behind. Such polar funnels could provide a favorable cite for the subsequent jets, which could attain high Lorentz factors pushed by the magnetic outflows and/or heated by neutrinos.
5. To obtain stronger neutrino energy deposition in the polar funnel heated from the accretion disk, we find that the smaller initial angular momentum is more appropriate. This is because the gravitational compression makes the temperature of the disk higher. When the accretion disk settles to the quasi-stationary state in their late time evolution, the maximum neutrino luminosity is found to reach $\sim 10^{52}$ erg/s. Due to the high neutrino opacity inside the disk, the luminosities of ν_e and $\bar{\nu}_e$ is found to become almost comparable, which is advantageous for making the deposition rate larger. Based on an order-of-magnitudes estimation of the energy deposition, it is suggested that the neutrino heating could be as efficient as the magnetic mechanism to energize the outflow. Among the computed models here, the model with the initial angular momentum of $j_{\text{crit}} \sim 1.5j_{\text{iso}}$ and with initial magnetic field strength of $B_0 \gtrsim 10^{10}$ G, provides the most plausible condition for collapsar, because such models are appropriate not only for producing the MHD outflows quickly by the magnetic towers, but also for obtaining the stronger neutrino heating in the evacuated polar funnel.

S.H. is grateful to T. Kajino for fruitful discussions. T.T. and K.K. express thanks to K. Sato and S. Yamada for continuing encouragements. Numerical computations were in part carried on XT4 and general common use computer system at the center for Computational Astrophysics, CfCA, the National Astronomical Observatory of Japan. This study was supported in part by the Grants-in-Aid for the Scientific Research from the Ministry of Education, Science and Culture of Japan (Nos. S19104006, 19540309 and 20740150).

Appendix A. Definition of energy

According to Takiwaki et al. (2009), we define special relativistic description of local energies as follows,

$$e_{\text{kin}} = \rho W (W - 1), \quad (\text{A1})$$

$$e_{\text{int}} = eW^2 + p(W^2 - 1), \quad (\text{A2})$$

$$e_{\text{Bi}} = \frac{B_i^2}{4\pi} \left(1 - \frac{1}{2W^2} \right), \quad (\text{A3})$$

$$e_{\text{mag}} = \sum_i e_{\text{Bi}}, \quad (\text{A4})$$

$$e_{\text{local}} = e_{\text{kin}} + e_{\text{int}} + e_{\text{mag}} + \Phi_{\text{tot}} \quad (\text{A5})$$

where e_{kin} is the total kinetic energy, e_{rot} is the rotational energy, e_{int} is the internal energy, e_{Bi} is the magnetic energy of i th component, e_{mag} is the total magnetic energy, and e_{local} is the total local energy. We use these values to compute the explosion energy of jets in §4.

Appendix B. Special relativistic treatments for neutrino cooling

Following the procedure in Mihalas & Mihalas (1984), we derive the neutrino cooling rates including special relativistic corrections. Neutrino emissivity is often calculated in the rest frame of relativistic fluids because radiation is usually isotropic there. When converting quantities in the rest frame to the laboratory (lab) frame in which the fluid variables are defined and evolved by the hydrodynamic equations, we need to take into account corrections from the Lorentz transformations between the two frames.

The cooling rate in the lab frame is calculated as follows,

$$q^- = \int \eta(\Omega, \epsilon) d\epsilon d\Omega, \quad (\text{B1})$$

by summing up the neutrino emissivity of $\eta(\Omega, \epsilon)$ (erg/cm³/s/str) of a neutrino energy of ϵ both over a solid angle $d\Omega$ and over $d\epsilon$ in the lab frame. To satisfy the number conservation under the Lorentz transformation, $(\eta/\epsilon)dt dV d\epsilon d\Omega$ is a Lorentz invariant. It is noted that the Lorentz transformation can be written in the following simple form (Mihalas & Mihalas

1984),

$$dtdV = dt_0dV_0 \quad (\text{B2})$$

$$d\epsilon = \frac{\epsilon}{\epsilon_0}d\epsilon_0 \quad (\text{B3})$$

$$d\Omega = \frac{\epsilon_0^2}{\epsilon^2}d\Omega_0 \quad (\text{B4})$$

$$\begin{aligned} \epsilon &= \gamma(1 + \beta\mu_0)\epsilon_0 \\ &= \epsilon_0/[\gamma(1 - \beta\mu)], \end{aligned} \quad (\text{B5})$$

where $\beta = |\mathbf{v}|/c$, $\gamma = (1 - \beta^2)^{-1/2}$, and $\mu = \mathbf{v} \cdot \mathbf{n}/|\mathbf{v}|$ where \mathbf{n} is the unit vector of the direction of the emitted neutrino. Here the subscript 0 denotes the variables which are measured in the rest frame. Then, we obtain the transformation of the emissivity,

$$\eta(\mu, \epsilon) = \frac{\epsilon^2}{\epsilon_0^2}\eta_0(\mu_0, \epsilon_0). \quad (\text{B6})$$

When the emission is isotropic in the rest frame, namely as

$$\eta_0(\mu_0, \epsilon_0) = \zeta_0(\epsilon_0), \quad (\text{B7})$$

where $\zeta_0(\epsilon_0)$ [erg/cm³/s] is the direction-averaged emissivity, the cooling rate in the lab frame can be given as,

$$\begin{aligned} q^- &= \int \eta(\Omega, \epsilon)d\epsilon d\Omega \\ &= \int \frac{\epsilon}{\epsilon_0}\eta_0(\mu_0, \epsilon_0)d\epsilon_0 d\Omega_0 \\ &= \int \left[\int \gamma(1 + \beta\mu_0) d\Omega_0 \right] \zeta_0(\epsilon_0)d\epsilon_0 \\ &= 4\pi\gamma \int \zeta_0(\epsilon_0)d\epsilon_0. \\ &= \gamma q_0^-. \end{aligned} \quad (\text{B8})$$

This equation means that the cooling rate becomes γ times larger than the one in the rest frame with the special relativistic effect. It is noted that this relation holds when $\eta_0(\mu_0, \epsilon_0)$ is isotropic in the rest frame, such as inside the accretion disk investigated here, which is very opaque to neutrinos and thus the radiation there is well approximated to be isotropic (see discussions in section 4.3).

Now we move on to consider the corrections to the opacity. Again from the number conservation with the Lorentz transformation of the absorption coefficient $\chi(\Omega, \nu)$ (erg/cm³/s/str),

$(\chi/\epsilon)dtdVded\Omega$ is a Lorentz invariant. Therefore, with the same approach in the case of the cooling, the absorption coefficient in the lab frame becomes,

$$\begin{aligned}\chi(\mu, \epsilon) &= \frac{\epsilon_0}{\epsilon} \chi_0(\mu_0, \epsilon_0) \\ &= \gamma(1 - \beta\mu) \chi_0(\mu_0, \epsilon_0).\end{aligned}\tag{B9}$$

Then the opacity can be calculated as,

$$\begin{aligned}d\tau &= \chi(\mu, \epsilon) ds \\ &= \gamma(1 - \beta\mu) \chi_0(\mu_0, \epsilon_0) ds \\ &= \gamma(1 - \beta\mu) d\tau_0,\end{aligned}\tag{B10}$$

where ds is the spatial distance in the lab frame. Here $(\gamma(1 - \beta\mu))$ reflects the special relativistic effect.

With the local cooling rate (Eq. (B8)) and the opacity (Eq. (B10)), we evaluated the effective cooling rate appeared in Eq. (3) as

$$\begin{aligned}\mathcal{L}_\nu &= q^- \exp\left[-\int d\tau\right] \\ &= \gamma q_0^- \exp\left[-\int \gamma(1 - \beta\mu) d\tau_0\right],\end{aligned}\tag{B11}$$

where the integration is performed along the radial direction for simplicity.

Finally, the reaction rate is also modified in the lab frame by the time contraction. The time evolution of Y_e is then given by

$$\begin{aligned}dY_e &= \Gamma_0 dt_0 \\ &= \Gamma_0 \gamma dt,\end{aligned}\tag{B12}$$

where Γ_0 represents the local neutrino reaction rates. Apparently, this modification could be important in the regions where the motion becomes (special)relativistic such as the inner most region of the disk or inside of the relativistic outflow.

Appendix C. Special relativistic modification for neutrino pair annihilation

Employing the same procedure as in the previous section, we here derive the heating rate via neutrino pair annihilation ($\nu + \bar{\nu} \rightarrow e^- + e^+$) with special relativistic corrections.

By putting the Lorentz transformations described in Eq.(B5) into the heating rate derived by previous studies (Salmonson & Wilson 1999; Asano & Fukuyama 2001), the heating rate in the lab frame is given by

$$\begin{aligned}
\frac{dq_{\nu\bar{\nu}}^+(\mathbf{r})}{dt dV} &= 2cKG_{\text{F}}^2 \int d\theta_{\nu} d\phi_{\nu} d\theta_{\bar{\nu}} d\phi_{\bar{\nu}} d\epsilon_{\nu} d\epsilon_{\bar{\nu}} \epsilon_{\nu}^2 \epsilon_{\bar{\nu}}^2 (\epsilon_{\nu} + \epsilon_{\bar{\nu}}) f_{\nu}(\mathbf{r}, \mathbf{p}_{\nu}) f_{\bar{\nu}}(\mathbf{r}, \mathbf{p}_{\bar{\nu}}) \\
&\times [1 - \sin\theta_{\nu} \sin\theta_{\bar{\nu}} \cos(\varphi_{\nu} - \varphi_{\bar{\nu}}) - \cos\theta_{\nu} \cos\theta_{\bar{\nu}}]^2 \sin\theta_{\nu} \sin\theta_{\bar{\nu}} \\
&= 2cKG_{\text{F}}^2 \int d\theta_{\nu} d\phi_{\nu} d\theta_{\bar{\nu}} d\phi_{\bar{\nu}} \\
&\times [SR_{\nu}^5(\Omega_{\nu}) SR_{\bar{\nu}}^4(\Omega_{\bar{\nu}}) S_{\nu,0}(\mathbf{r}, \Omega_{\nu}) N_{\bar{\nu},0}(\mathbf{r}, \Omega_{\bar{\nu}}) \\
&\quad + SR_{\nu}^4(\Omega_{\nu}) SR_{\bar{\nu}}^5(\Omega_{\bar{\nu}}) N_{\nu,0}(\mathbf{r}, \Omega_{\nu}) S_{\bar{\nu},0}(\mathbf{r}, \Omega_{\bar{\nu}})] \\
&\times [1 - \sin\theta_{\nu} \sin\theta_{\bar{\nu}} \cos(\varphi_{\nu} - \varphi_{\bar{\nu}}) - \cos\theta_{\nu} \cos\theta_{\bar{\nu}}]^2 \sin\theta_{\nu} \sin\theta_{\bar{\nu}}, \quad (\text{C1})
\end{aligned}$$

where

$$\begin{aligned}
SR_{\nu}(\mathbf{r}, \Omega_{\nu}) &= \epsilon_{\nu} / \epsilon_{\nu,0} \\
&= 1 / [\gamma_{\nu} (1 - \mu_{\nu} \beta_{\nu})], \quad (\text{C2})
\end{aligned}$$

$$\beta_{\nu} = \frac{|\mathbf{v}_{\nu}|}{c}, \quad (\text{C3})$$

$$\gamma_{\nu} = \frac{1}{\sqrt{1 - \beta_{\nu}^2}}, \quad (\text{C4})$$

$$\mu_{\nu} = \frac{\mathbf{n}_{\nu} \cdot \mathbf{v}_{\nu}}{|\mathbf{v}_{\nu}|} \quad (\text{C5})$$

$$\mathbf{n}_{\nu} = \frac{\mathbf{p}_{\nu}}{|\mathbf{p}_{\nu}|} = (\sin\theta_{\nu} \cos\phi_{\nu}, \sin\theta_{\nu} \sin\phi_{\nu}, \cos\theta_{\nu}), \quad (\text{C6})$$

$$S_{\nu,0}(\mathbf{r}, \Omega_{\nu}) = \int \epsilon_{\nu,0}^4 f_{\nu,0}(\mathbf{r}_{\nu,0}, \mathbf{p}_{\nu,0}) d\epsilon_{\nu,0}, \quad (\text{C7})$$

$$N_{\nu,0}(\mathbf{r}, \Omega_{\nu}) = \int \epsilon_{\nu,0}^3 f_{\nu,0}(\mathbf{r}_{\nu,0}, \mathbf{p}_{\nu,0}) d\epsilon_{\nu,0}, \quad (\text{C8})$$

and $\mathbf{r}_{\nu}, \mathbf{v}_{\nu}, \mathbf{p}_{\nu}, f_{\nu}$ denotes the position of the neutrino source, the velocity of fluid at the neutrino source, the momentum vector of neutrino, and the distribution function of neutrino. Definitions are same for the anti-electron type neutrino by changing the notation ν to $\bar{\nu}$ from Eq.(C2) to Eq.(C8). Subscript 0 again denotes variables which are measured in the rest frame of the neutrino source. Here the neutrino source indicates the accretion disk. The neutrino number flux along its path to the target is assumed to be conserved for simplicity as $f_{\nu}(\mathbf{r}, \mathbf{p}_{\nu}) = f_{\nu}(\mathbf{r}_{\nu,0}, \mathbf{p}_{\nu,0})$. In Eq.(C1), the factor SR_{ν} reflects the special relativistic modification to the heating rate.

The neutrino distribution function inside the accretion is well approximated by the one

in the β equilibrium as,

$$\begin{aligned} f_\nu(\mathbf{r}_{\nu,0}, \mathbf{p}_{\nu,0}) &= \frac{1}{(hc)^3} \frac{dn_0}{d\epsilon_0 d\Omega_0 dt_0 dV_0} \\ &= \frac{1}{(hc)^3} \frac{1}{\exp(\epsilon_{\nu,0}/kT_{\nu,0} - \eta_{\nu,0}) + 1}, \end{aligned} \quad (\text{C9})$$

where $T_{\nu,0}$, $\eta_{\nu,0}$ is the temperature and degeneracy parameter of neutrino in the rest frame, respectively. We approximate $T_{\nu,0}$ to be equal to the temperature of fluid $T(\mathbf{r}_\nu)$. Then, S and N in Eq. (C1) can be expressed by the Fermi integrals \mathcal{F}_k as

$$\mathcal{F}_k(y) \equiv \int_0^\infty \frac{x^k}{\exp(x - y) + 1} dx, \quad (\text{C10})$$

$$S_{\nu,0}(\mathbf{r}, \Omega) = \frac{(kT(\mathbf{r}_\nu))^5}{(hc)^3} \mathcal{F}_4(\eta_{\nu,0}), \quad (\text{C11})$$

$$N_{\nu,0}(\mathbf{r}, \Omega) = \frac{(kT(\mathbf{r}_\nu))^4}{(hc)^3} \mathcal{F}_3(\eta_{\nu,0}). \quad (\text{C12})$$

With these modifications, we calculated the heating rate in section 5.2.

REFERENCES

- Abramowicz, M. A., Beloborodov, A. M., Chen, X.-M., & Igumenshchev, I. V. 1996, *A&A*, 313, 334
- Aloy, M. A., Müller, E., Ibáñez, J. M., Martí, J. M., & MacFadyen, A. 2000, *ApJ*, 531, L119
- Asano, K. & Fukuyama, T. 2000, *ApJ*, 531, 949
- . 2001, *ApJ*, 546, 1019
- Balbus, S. A. & Hawley, J. F. 1998, *Reviews of Modern Physics*, 70, 1
- Barkov, M. V. & Komissarov, S. S. 2008, *MNRAS*, 385, L28
- Birkl, R., Aloy, M. A., Janka, H.-T., & Müller, E. 2007, *A&A*, 463, 51
- Blinnikov, S. I., Dunina-Barkovskaya, N. V., & Nadyozhin, D. K. 1996, *ApJS*, 106, 171
- Burrows, A., Dessart, L., Livne, E., Ott, C. D., & Murphy, J. 2007, *ApJ*, 664, 416
- De Villiers, J.-P., Hawley, J. F., & Krolik, J. H. 2003, *ApJ*, 599, 1238

- De Villiers, J.-P., Hawley, J. F., Krolik, J. H., & Hirose, S. 2005, *ApJ*, 620, 878
- Dessart, L., Burrows, A., Livne, E., & Ott, C. D. 2008, *ApJ*, 673, L43
- Detmers, R. G., Langer, N., Podsiadlowski, P., & Izzard, R. G. 2008, *A&A*, 484, 831
- Epstein, R. I. & Pethick, C. J. 1981, *ApJ*, 243, 1003
- Fujimoto, S.-i., Kotake, K., Yamada, S., Hashimoto, M.-a., & Sato, K. 2006, *ApJ*, 644, 1040
- Fukue, J. 2004, *PASJ*, 56, 681
- Fuller, G. M., Fowler, W. A., & Newman, M. J. 1985, *ApJ*, 293, 1
- Gal-Yam, A., Fox, D. B., Price, P. A., Ofek, E. O., Davis, M. R., Leonard, D. C., Soderberg, A. M., Schmidt, B. P., Lewis, K. M., Peterson, B. A., Kulkarni, S. R., Berger, E., Cenko, S. B., Sari, R., Sharon, K., Frail, D., Moon, D.-S., Brown, P. J., Cucchiara, A., Harrison, F., Piran, T., Persson, S. E., McCarthy, P. J., Penprase, B. E., Chevalier, R. A., & MacFadyen, A. I. 2006, *Nature*, 444, 1053
- Galama, T. J., Vreeswijk, P. M., van Paradijs, J., Kouveliotou, C., Augusteijn, T., Bönhardt, H., Brewer, J. P., Doublier, V., Gonzalez, J.-F., Leibundgut, B., Lidman, C., Hainaut, O. R., Patat, F., Heise, J., in't Zand, J., Hurley, K., Groot, P. J., Strom, R. G., Mazzali, P. A., Iwamoto, K., Nomoto, K., Umeda, H., Nakamura, T., Young, T. R., Suzuki, T., Shigeyama, T., Koshut, T., Kippen, M., Robinson, C., de Wildt, P., Wijers, R. A. M. J., Tanvir, N., Greiner, J., Pian, E., Palazzi, E., Frontera, F., Masetti, N., Nicastro, L., Feroci, M., Costa, E., Piro, L., Peterson, B. A., Tinney, C., Boyle, B., Cannon, R., Stathakis, R., Sadler, E., Begam, M. C., & Ianna, P. 1998, *Nature*, 395, 670
- Gehrels, N., Norris, J. P., Barthelmy, S. D., Granot, J., Kaneko, Y., Kouveliotou, C., Markwardt, C. B., Mészáros, P., Nakar, E., Nousek, J. A., O'Brien, P. T., Page, M., Palmer, D. M., Parsons, A. M., Roming, P. W. A., Sakamoto, T., Sarazin, C. L., Schady, P., Stamatikos, M., & Woosley, S. E. 2006, *Nature*, 444, 1044
- Ghisellini, G., Ghirlanda, G., & Tavecchio, F. 2007, *MNRAS*, L117+
- Hawley, J. F. & Krolik, J. H. 2006, *ApJ*, 641, 103
- Hjorth, J., Sollerman, J., Møller, P., Fynbo, J. P. U., Woosley, S. E., Kouveliotou, C., Tanvir, N. R., Greiner, J., Andersen, M. I., Castro-Tirado, A. J., Castro Cerón, J. M., Fruchter, A. S., Gorosabel, J., Jakobsson, P., Kaper, L., Klose, S., Masetti, N., Pedersen, H., Pedersen, K., Pian, E., Palazzi, E., Rhoads, J. E., Rol, E., van den

- Heuvel, E. P. J., Vreeswijk, P. M., Watson, D., & Wijers, R. A. M. J. 2003, *Nature*, 423, 847
- Janiuk, A., Moderski, R., & Proga, D. 2008, *ApJ*, 687, 433
- Janiuk, A. & Proga, D. 2008, *ApJ*, 675, 519
- Kawagoe, S., Takiwaki, T., & Kotake, K. 2009, ArXiv e-prints
- Komissarov, S. S. & McKinney, J. C. 2007, *MNRAS*, 377, L49
- Kotake, K., Iwakami, W., Ohnishi, N., & Yamada, S. 2009, *ApJ*, 697, L133
- Kotake, K., Sato, K., & Takahashi, K. 2006, *Reports on Progress in Physics*, 69, 971
- Kotake, K., Sawai, H., Yamada, S., & Sato, K. 2004, *ApJ*, 608, 391
- Kotake, K., Yamada, S., & Sato, K. 2003, *ApJ*, 595, 304
- Lattimer, J. M. & Prakash, M. 2001, *ApJ*, 550, 426
- Lee, W. H. & Ramirez-Ruiz, E. 2006, *ApJ*, 641, 961
- Lopez-Camara, D., Lee, W. H., & Ramirez-Ruiz, E. 2009, *ApJ*, 692, 804
- Lynden-Bell, D. 1996, *MNRAS*, 279, 389
- . 2003, *MNRAS*, 341, 1360
- MacFadyen, A. I. & Woosley, S. E. 1999, *ApJ*, 524, 262
- McKinney, J. C. 2006, *MNRAS*, 367, 1797
- McKinney, J. C. & Narayan, R. 2007, *MNRAS*, 375, 531
- Meszaros, P. 2006, *Reports of Progress in Physics*, 69, 2259
- Mihalas, D. & Mihalas, B. W. 1984
- Mizuno, Y., Hardee, P., & Nishikawa, K.-I. 2007, *ApJ*, 662, 835
- Mizuno, Y., Nishikawa, K.-I., Koide, S., Hardee, P., & Fishman, G. J. 2006, ArXiv Astrophysics e-prints
- Montero, P. J., Font, J. A., & Shibata, M. 2008, *Phys. Rev. D*, 78, 064037
- Mościbrodzka, M. & Proga, D. 2009, *MNRAS*, 865

- Nagataki, S. 2009, ArXiv e-prints
- Nagataki, S., Takahashi, R., Mizuta, A., & Takiwaki, T. 2007, *ApJ*, 659, 512
- Nakar, E. 2007, *Phys. Rep.*, 442, 166
- Obergaulinger, M., Aloy, M. A., Dimmelmeier, H., & Müller, E. 2006, *A&A*, 457, 209
- Ott, C. D. 2009, *Classical and Quantum Gravity*, 26, 063001
- Paczynski, B. 1998, *ApJ*, 494, L45+
- Paczynsky, B. & Wiita, P. J. 1980, *A&A*, 88, 23
- Piran, T. 1999, *Phys. Rep.*, 314, 575
- Piro, L., Amati, L., Antonelli, L. A., Butler, R. C., Costa, E., Cusumano, G., Feroci, M., Frontera, F., Heise, J., in 't Zand, J. J. M., Molendi, S., Muller, J., Nicastro, L., Orlandini, M., Owens, A., Parmar, A. N., Soffitta, P., & Tavani, M. 1998, *A&A*, 331, L41
- Proga, D. 2005, *ApJ*, 629, 397
- Proga, D., MacFadyen, A. I., Armitage, P. J., & Begelman, M. C. 2003a, *ApJ*, 582, 69
- . 2003b, *ApJ*, 599, L5
- Proga, D. & Zhang, B. 2006, *MNRAS*, 370, L61
- Proga, D. and Begelman, M. C. 2003, *ApJ*, 592, 767
- Rosswog, S. & Liebendörfer, M. 2003, *MNRAS*, 342, 673
- Salmonson, J. D. & Wilson, J. R. 1999, *ApJ*, 517, 859
- Savaglio, S., Glazebrook, K., & Le Borgne, D. 2006, in *American Institute of Physics Conference Series*, Vol. 836, *Gamma-Ray Bursts in the Swift Era*, ed. S. S. Holt, N. Gehrels, & J. A. Nousek, 540–545
- Sawai, H., Kotake, K., & Yamada, S. 2005, *ApJ*, 631, 446
- Sekiguchi, Y. & Shibata, M. 2007, *Progress of Theoretical Physics*, 117, 1029
- Shen, H., Toki, H., Oyamatsu, K., & Sumiyoshi, K. 1998, *Nuclear Physics A*, 637, 435
- Shibata, M., Liu, Y. T., Shapiro, S. L., & Stephens, B. C. 2006, *Phys. Rev. D*, 74, 104026

- Shibata, M., Sekiguchi, Y., & Takahashi, R. 2007, *Progress of Theoretical Physics*, 118, 257
- Soderberg, A. M., Kulkarni, S. R., Nakar, E., Berger, E., Cameron, P. B., Fox, D. B., Frail, D., Gal-Yam, A., Sari, R., Cenko, S. B., Kasliwal, M., Chevalier, R. A., Piran, T., Price, P. A., Schmidt, B. P., Pooley, G., Moon, D.-S., Penprase, B. E., Ofek, E., Rau, A., Gehrels, N., Nousek, J. A., Burrows, D. N., Persson, S. E., & McCarthy, P. J. 2006, *Nature*, 442, 1014
- Stanek, K. Z., Gnedin, O. Y., Beacom, J. F., Gould, A. P., Johnson, J. A., Kollmeier, J. A., Modjaz, M., Pinsonneault, M. H., Pogge, R., & Weinberg, D. H. 2006, *Acta Astronomica*, 56, 333
- Stanek, K. Z., Matheson, T., Garnavich, P. M., Martini, P., Berlind, P., Caldwell, N., Challis, P., Brown, W. R., Schild, R., Krisciunas, K., Calkins, M. L., Lee, J. C., Hathi, N., Jansen, R. A., Windhorst, R., Echevarria, L., Eisenstein, D. J., Pindor, B., Olszewski, E. W., Harding, P., Holland, S. T., & Bersier, D. 2003, *ApJ*, 591, L17
- Suwa, Y., Takiwaki, T., Kotake, K., & Sato, K. 2007, *PASJ*, 59, 771
- Takahashi, K., El Eid, M. F., & Hillebrandt, W. 1978, *A&A*, 67, 185
- Takiwaki, T., Kotake, K., Nagataki, S., & Sato, K. 2004, *ApJ*, 616, 1086
- Takiwaki, T., Kotake, K., & Sato, K. 2009, *ApJ*, 691, 1360
- Thompson, T. A., Chang, P., & Quataert, E. 2004, *ApJ*, 611, 380
- Uzdensky, D. A. & MacFadyen, A. I. 2007a, *ApJ*, 669, 546
- . 2007b, *Physics of Plasmas*, 14, 6506
- Vink, J. S. & de Koter, A. 2005, *A&A*, 442, 587
- Wheeler, J. C., Yi, I., Höflich, P., & Wang, L. 2000, *ApJ*, 537, 810
- Woosley, S. E. 1993, *ApJ*, 405, 273
- Woosley, S. E. & Heger, A. 2006, *ApJ*, 637, 914
- Yoon, S.-C. & Langer, N. 2005, *A&A*, 443, 643
- Zhang, W. & MacFadyen, A. 2009, *ApJ*, 698, 1261
- Zhang, W., Woosley, S. E., & Heger, A. 2008, *ApJ*, 679, 639

Zhang, W., Woosley, S. E., & MacFadyen, A. I. 2003, ApJ, 586, 356

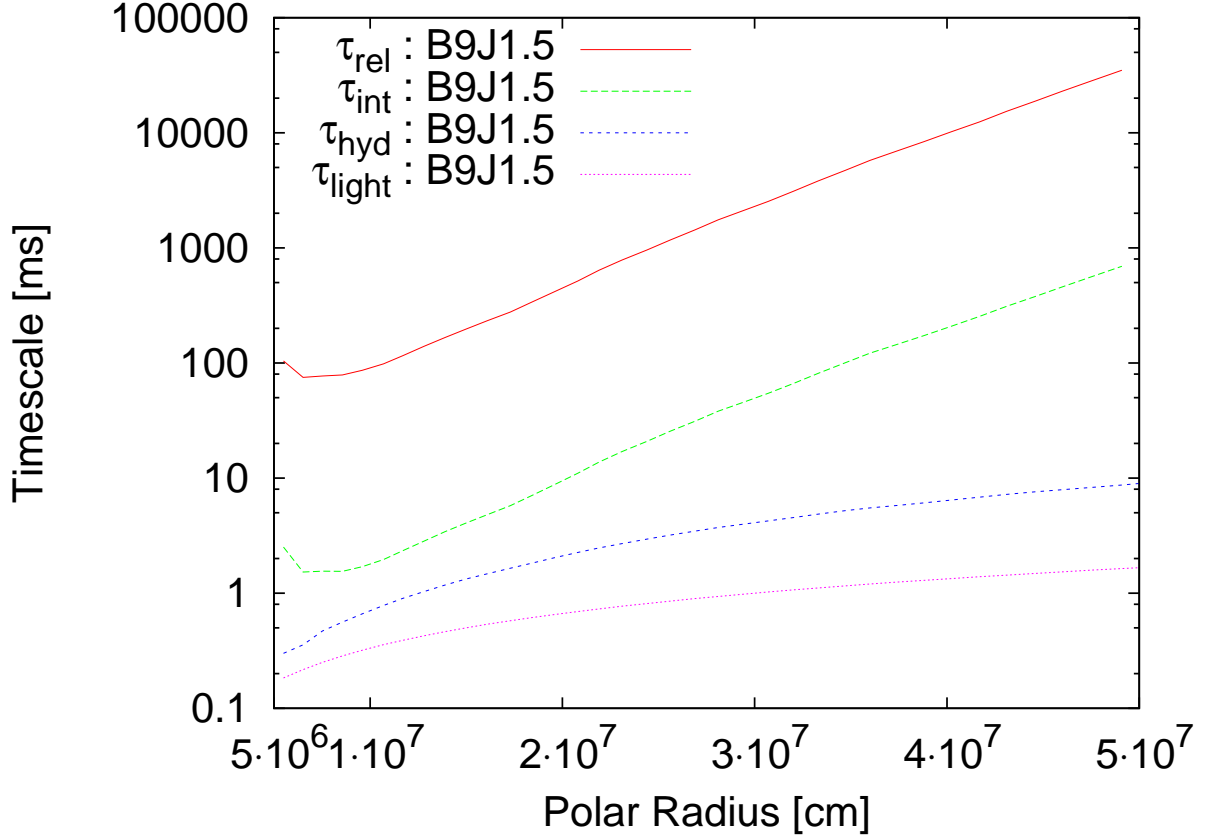


Fig. 15.— Plots of various timescale for matter ; the timescale to get relativistic by the neutrino heating τ_{rel} (solid), the timescale to affect dynamics with neutrino heating τ_{int} (dashed), the timescale of dynamical motion τ_{hyd} (dotted), and the timescale of light crossing τ_{light} (small dotted), at 9.22 s when the accretion disk reaches to the stationary state with the funnel regions along the pole.

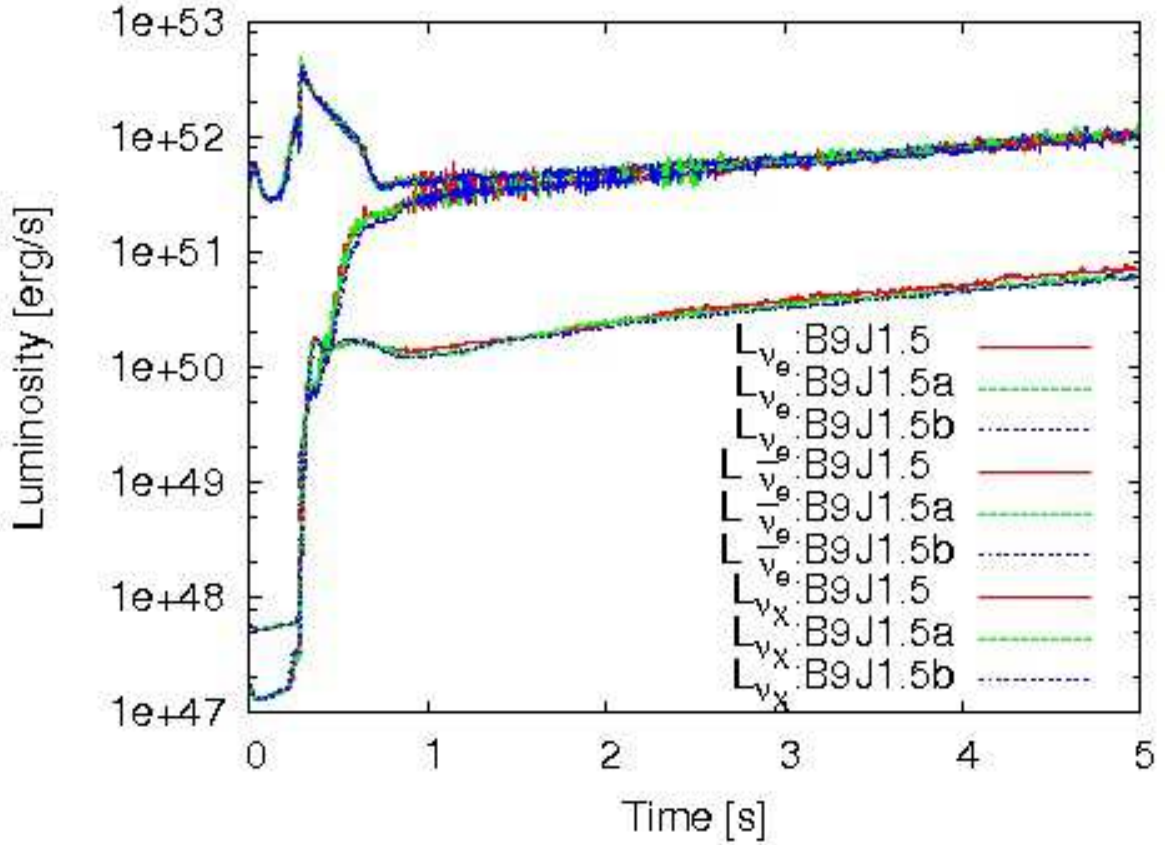


Fig. 16.— Time evolution of neutrino luminosities of ν_e (solid line), $\bar{\nu}_e$ (dashed line), and ν_X (dotted line) for model B9J1.5. Models labeled by “a” and “b” have doubled mesh points in the radial and azimuthal directions than the canonical one of $300(r) \times 40(\theta)$ mesh points. Each luminosity coincides well with each other, showing the numerical convergence of the obtained results.

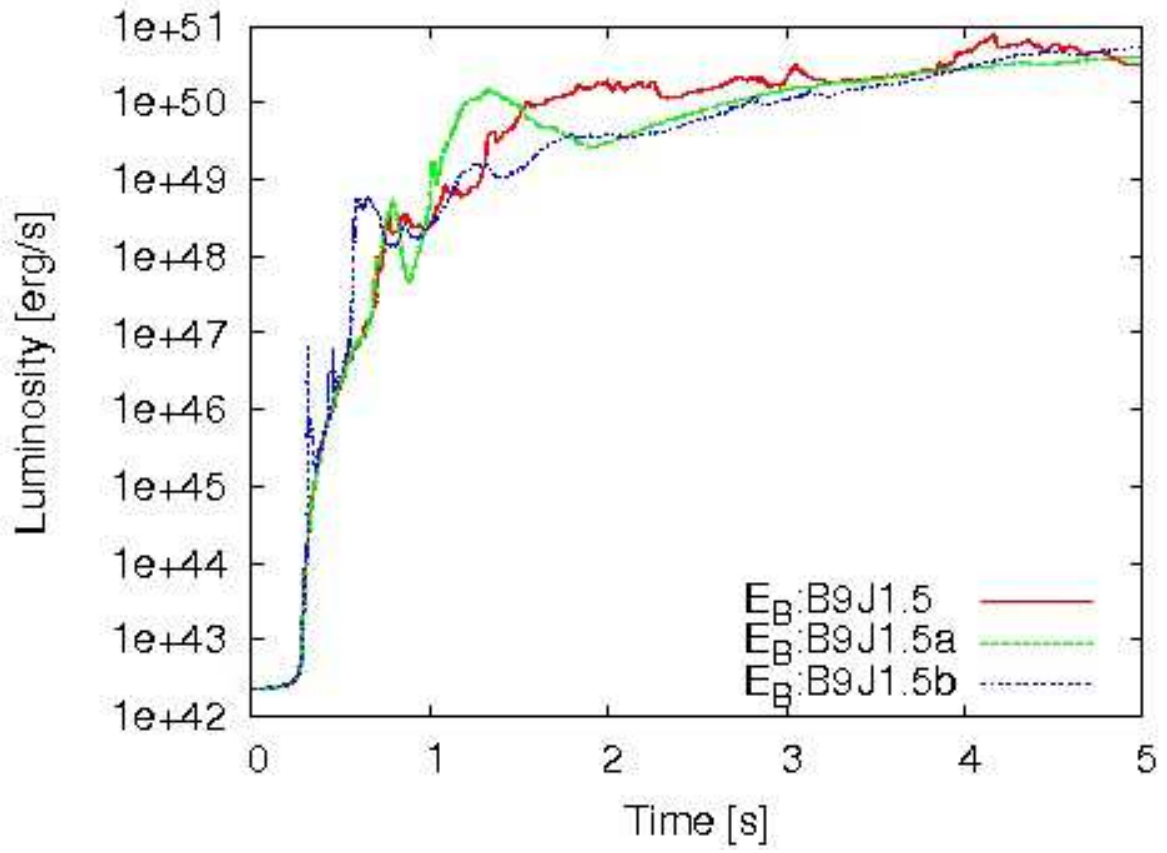


Fig. 17.— Same as Figure 16 but for the time evolution of magnetic energy.

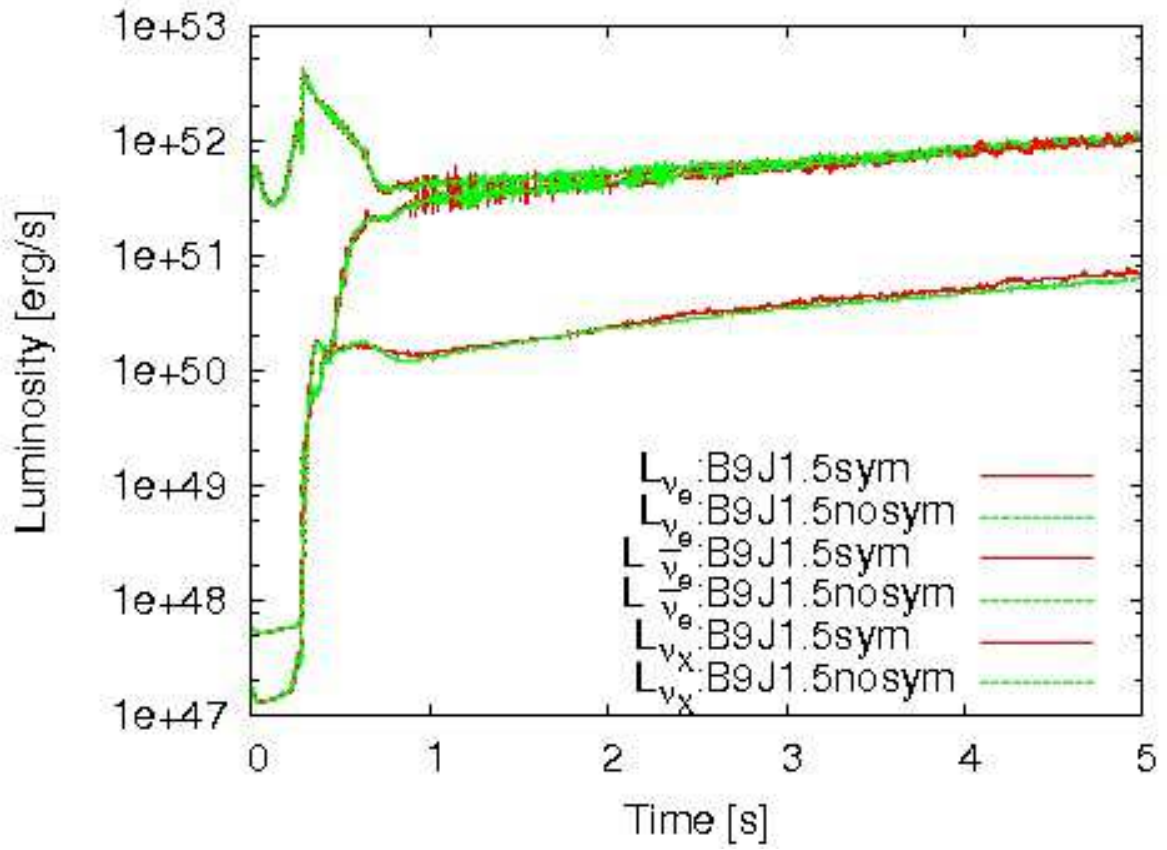


Fig. 18.— Same as Figure 16 but with and without equatorial symmetry (indicated by “sym” and “no sym”, respectively).

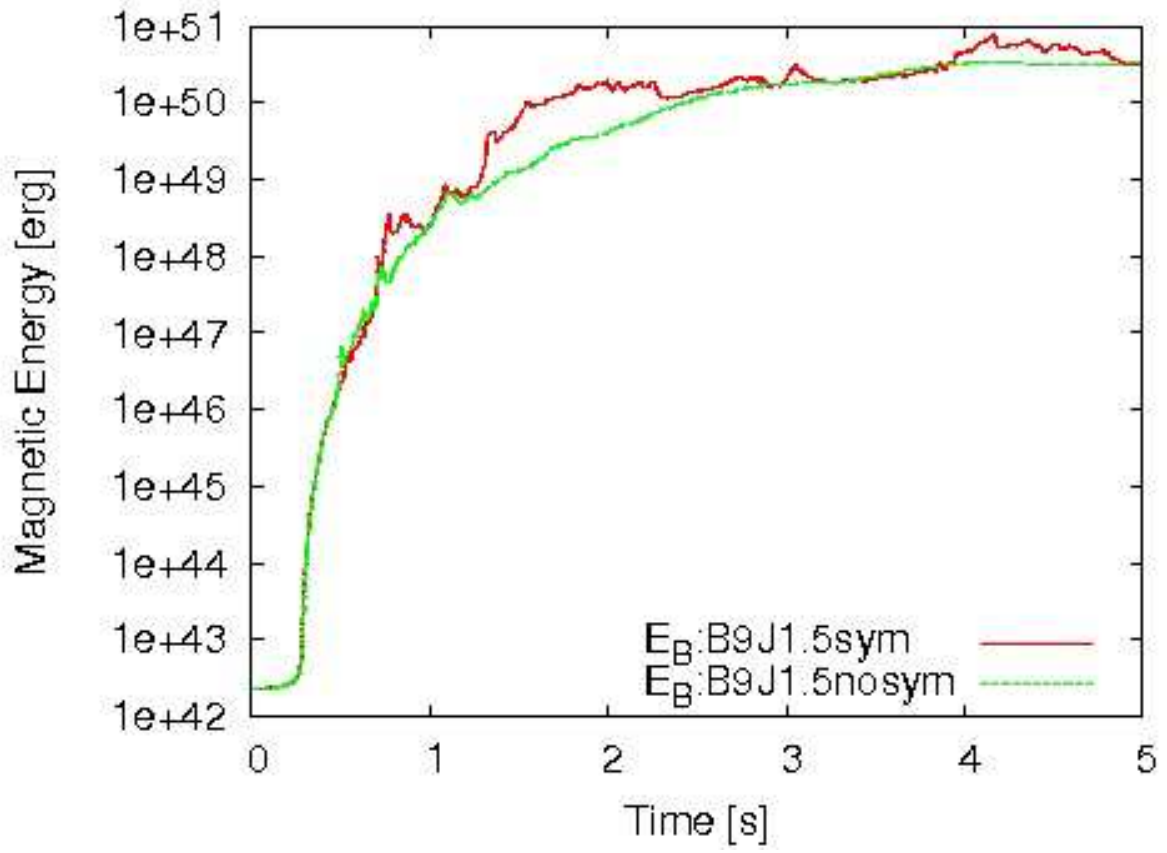


Fig. 19.— Same as Figure 18 but for the time evolution of magnetic energy.